Marianne Diniz Rocha Henriques

Evolution of point defects in $Al_2W_3O_{12}$ during calcination in air and the effects of different sintering methods on its density, microstructure, and hardness

Dissertação de Mestrado

Dissertation presented to the Programa de Pós-Graduação em Engenharia Química, de Materiais e Processos Ambientais in partial fulfillment of the requirements for the degree of Mestre em Engenharia Química, de Materiais e Processos Ambientais

Advisor: Prof. Bojan A. Marinkovic

Rio de Janeiro
March 2024

PONTIFÍCIA UNIVERSIDADE CATÓLICA
DO RIO DE JANEIRO

Marianne Diniz Rocha Henriques

Evolution of point defects in $Al_2W_3O_{12}$ during calcination in air and the effects of different sintering methods on its density, microstructure and hardness

Dissertation presented to the Programa de Pós-graduação em Engenharia Química, de Materiais e Processos Ambientais of PUC-Rio in partial fulfillment of the requirements for the degree of Mestre em Engenharia Química, de Materiais e Processos Ambientais. Approved by the Examination Committee.

Prof. Bojan Marinkovic
Departamento de Engenharia Química e de Materiais - PUC-Rio

Prof. Roberto Ribeiro de Avillez
Departamento de Engenharia Química e de Materiais - PUC-Rio

Prof. Marcello Filgueira
Universidade Estadual do Norte Fluminense Darcy Ribeiro - UENF

Rio de Janeiro, March 11th, 2024

Marianne Diniz Rocha Henriques

Undergrad in Physics by the Federal Fluminense University – UFF in 2021. Areas of interest: Production and characterization of nanomaterials.

Bibliographic data

Henriques, Marianne Diniz Rocha

Evolution of point defects in $Al_2W_3O_{12}$ during calcination in air and the effects of different sintering methods on its density, microstructure, and hardness / Marianne Diniz Rocha Henriques ; advisor: Bojan A. Marinkovic. – 2024.

97 f. : il. color. ; 30 cm

Dissertação (mestrado)–Pontifícia Universidade Católica do Rio de Janeiro, Departamento de Engenharia Química e de Materiais, 2024.

Inclui bibliografia

1. Engenharia Química e de Materiais – Teses. 2. $A_2M_3O_{12}$. 3. $Al_2(WO_4)_3$. 4. Vacâncias de oxigênio. 5. Spark plasma sintering. 6. Sinterização rápida sem auxílio de pressão. I. Marinkovic, Bojan A. II. Pontifícia Universidade Católica do Rio de Janeiro. Departamento de Engenharia Química e de Materiais. III. Título.

CDD: 620.11

In memory of my grandmother, Irinea Diniz.
To my loved ones, for their support and
encouragement.
To Luna.
To my love, Thiago Gabrig.

Acknowledgments

I would like to express my deepest appreciation to my boyfriend, Thiago Gabrig, for his love, support, and understanding throughout this journey. I would also like to express my gratitude to my friends, Tamires, Jessica, Pudim, and Yngrid, but especially to Laura for the friendship, support, kindness, and companionship along the way. I'm also grateful for my family's love and support in this life and the next.

I would like to thank everyone on the research group Cepecam I'm part of, Juliana, Lais, Lucas, Emanuel, Esteban, Allan, and Vinicius for the partnership. My gratitude to the chemistry lab LabSpectro for the ICP measurements (although not used in this study), availability, and kindness, especially the technicians Rodrigo and Mauricio.

My forever gratitude to my advisor, prof. Bojan Marinkovic, for the work, meetings, and trust throughout the development of this study.

I'm extremely grateful to the research institute CEITEC in Brno, Czech Republic, especially Vojtěch Marak, Daniel Drdlík, and Prof. Karel Maca, for the internship that allowed this study to prevail, and for the SPS and RPLS measurements, SEM micrographs, Raman, and XPS spectroscopies. In the same manner, I would like to thank Vinicius Santana for the EPR measurements performed in the same institute. My deepest gratitude to Vojtěch Marak for the friendship, support, and all the help during this time.

My gratitude to Prof. Paula Jardim and Thaissa (UFRJ) for TEM images and sample preparation.

I would also like to thank the examiner's board for accepting to evaluate my work.

This study was financed in part by the Coordenação de Aperfeiçoaento de Pessoal de Nível Superior - Brasil (CAPES) - Finance Code 001.

This study was financed in part by the U.S. Army Research Laboratory.

Abstract

Diniz Rocha Henriques, Marianne; Marinkovic, Bojan (Advisor). **Evolution of point defects in $Al_2W_3O_{12}$ during calcination in air and the effects of different sintering methods on its density, microstructure, and hardness.** Rio de Janeiro, 2024. 97p. Dissertação de Mestrado – Departamento de Engenharia Química e de Materiais, Pontifícia Universidade Católica do Rio de Janeiro.

This work consists of two complementary studies regarding $Al_2W_3O_{12}$-based materials. Therefore, the aim of this work was to i) produce dense $Al_2W_3O_{12}$ ceramics by different sintering routes and evaluate its effects on densification and microstructure, and ii) evaluate the evolution of point defects on $Al_2W_3O_{12}$ after temperature variations during the calcination process in air atmosphere. $Al_2W_3O_{12}$ amorphous powder was produced *via* coprecipitation synthesis followed by calcination to induce crystallization. The influence of the different calcination temperatures in ambient air atmosphere was assessed while the calcination time remained the same, by various techniques, such as X-ray Powder Diffraction (XRPD), Raman, and Electron Paramagnetic Resonance (EPR) Spectroscopies to understand the formation of point defects into $Al_2W_3O_{12}$ crystal structure. Different concentrations of oxygen vacancies were formed while altering the calcination temperature from 500 – 620 ºC. It was observed that the oxygen vacancy concentration increases with the decrease of the calcination temperature. Interestingly, the highest oxygen vacancy content occurs while the powder is still amorphous at 500 ºC. Therefore, the crystallization process of orthorhombic $Al_2W_3O_{12}$ is highly affected by the formation of oxygen vacancies. The best $Al_2W_3O_{12}$ powder, calcined at 570 ºC, was selected and used to consolidate the pellets for sintering. It was determined that due to the presence of agglomerates, further milling was necessary to break the agglomerates and increase the specific surface area of the powder. After ball-milling the specific surface area went from 26.4 m^2g^{-1} to 31.4 m^2g^{-1}. The milled and non-milled calcined powders were used to produce sintered bodies and is densification, microstructure, and mechanical properties compared. The sintering routes consisted of Rapid Pressure-Less Sintering (RPLS) technique and Spark Plasma Sintering method (SPS). RPLS technique produced dense cylinders of 96 % density at its best setting, while SPS produced pellets as dense as 98.8 % TD. The process of milling the calcined powder did not show much improvement in either densification or microstructure, forming samples slightly denser than those without milling.

Keywords

$A_2M_3O_{12}$; $Al_2(WO_4)_3$; coprecipitation; oxygen vacancy; spark plasma sintering; rapid pressure-less sintering.

Resumo

Diniz Rocha Henriques, Marianne; Marinkovic, Bojan (Advisor). **Evolução do estado de defeitos pontuais na $Al_2W_3O_{12}$ durante calcinação ao ar e o efeito de diferentes métodos de sinterização sobre sua densidade e microestrutura.** Rio de Janeiro, 2024. 97p. Dissertação de Mestrado – Departamento de Engenharia Química e de Materiais, Pontifícia Universidade Católica do Rio de Janeiro.

Este trabalho consiste em dois estudos complementares sobre materiais a base de $Al_2W_3O_{12}$. Portanto, o objetivo deste trabalho foi i) produzir cerâmicas densas de $Al_2W_3O_{12}$ através de diferentes métodos de sinterização e avaliar sua densificação e microestrutura, e ii) avaliar a evolução do estado dos defeitos pontuais no $Al_2W_3O_{12}$ depois de variações de temperatura durante o processo de calcinação em ar. Pó amorfo de $Al_2W_3O_{12}$ foi produzido via coprecipitação seguido por calcinação para induzir cristalização. A influência das diferentes temperaturas de calcinação em atmosfera de ar ambiente foi verificada enquanto o tempo de calcinação se manteve fixo, por diferentes técnicas, como Difração de Raios-X (DRX), espectroscopia Raman, e espectroscopia de Ressonância Paramagnética Eletrônica (EPR), para entender a formação de defeitos pontuais na estrutura cristalina do $Al_2W_3O_{12}$. Diferentes concentrações de vacâncias de oxigênio foram formadas ao alterar a temperatura de calcinação de 500 a 620 ºC. Foi observado que a concentração de vacâncias de oxigênio aumenta com a redução da temperatura de calcinação. Interessantemente, a maior concentração de vacâncias de oxigênio ocorre enquanto o pó ainda é amorfo à 500 ºC. Portanto, o processo de cristalização do $Al_2W_3O_{12}$ ortorrômbico é altamente afetado pela formação de vacâncias de oxigênio. O melhor pó de $Al_2W_3O_{12}$, calcinado a 570 ºC, foi selecionado e utilizado para consolidação das pastilhas para sinterização. Foi determinado que devido a presença de aglomerados, foi necessário moagem para quebrar os aglomerados e aumentar a área superficial específica do pó. Após moagem de bolas a área superficial específica foi de 26.4 m^2g^{-1} para 31.4 m^2g^{-1}. Os pós calcinados moídos e não moídos foram usados para produzir corpos de prova sinterizados, e a sua densificação, microestrutura e propriedades mecânicas foram comparadas. As rotas de sinterização consistem em Sinterização Rápida Sem Auxílio de Pressão (RPLS) e Spark Plasma Sintering method (SPS). O método RPLS produziu cerâmicas densas de 96 % da densidade teórica em sua melhor configuração, enquanto SPS produzir pastilhas tão densas quanto 98 % da densidade teórica. O processo de moagem dos pós calcinados não mostrou grande melhora na densificação ou microestrutura, formando amostras ligeiramente mais densas do que aquelas sem moagem.

Palavras-chave

$A_2M_3O_{12}$; $Al_2(WO_4)_3$; coprecipitação; vacâncias de oxigênio; spark plasma sintering; sinterização rápida sem auxílio de pressão.

Table of Contents

1. Introduction 17

2. Literature Review 19

2.1 Thermal expansion 19

2.1.1 Coefficient of Thermal Expansion – CTE 20

2.1.2 Negative Thermal Expansion 21

2.2 $A_2M_3O_{12}$ family 23

2.2.1 Synthesis of $A_2M_3O_{12}$ 24

2.2.1.1 Co-precipitation principles 25

2.3 Point defects in ceramics 26

2.3.1 Point defects notation for ionic compounds 28

2.3.2 Oxygen vacancy formation 29

2.4 Sintering 31

2.4.1 Rapid Pressure-Less Sintering – RPLS 33

2.4.2 Spark Plasma Sintering – SPS 34

3. Objectives 37

3.1 General objectives 37

3.1.1 General objectives of the first scope 37

3.1.2 General objectives of the second scope 37

3.2 Specific objectives 37

3.2.1 Specific objectives of the first scope 37

3.2.2 Specific objectives of the second scope 37

4. Extrinsic oxygen vacancies formation during crystallization of $Al_2W_3O_{12}$ by calcination in air 39

4.1 Introduction 39

4.2 Materials and Methods 42

4.2.1 Synthesis of $Al_2W_3O_{12}$ 42

4.2.2 Characterization 43

4.3 Results and Discussion 44

4.3.1 Crystallization study 44

4.3.2 Optical properties study 48

4.3.3 Oxygen vacancies study and volumetric expansion calculation 50

4.3.4 Charge compensation study 55

4.4 Conclusions and Future works 58

5. Rapid densification of low positive thermal expansion $Al_2W_3O_{12}$ ceramics 60

5.1 Introduction 60

5.2 Materials and Methods 62

5.2.1 Synthesis of $Al_2W_3O_{12}$ 62

5.2.2 Characterization 62

5.2.3 Sintering 63

5.3 Results and Discussion 64

5.3.1 $Al_2W_3O_{12}$ powders and green bodies 64

5.3.2 Dilatometry 67

5.3.3 Densification of $Al_2W_3O_{12}$ and phase composition 68

5.3.4 Microstructure and grain area distribution 70

5.3.5 Coefficient of Thermal Expansion – CTE 73

5.3.6 Mechanical properties 75

5.4 Conclusions and Future works 76

6. Appendix 77

6.1 Supplementary information of chapter 4 77

7. References 84

List of Figures

Figure 1 – Diagram of an asymmetric potential energy well [1] 19

Figure 2 – Longitudinal and transverse vibrations of M-O-M links [2] 21

Figure 3 – Schematic representation of a) transverse vibrational modes of M-O-M links, and b) rotation mechanisms of polyhedra [17] 22

Figure 4 – Orthorhombic crystal structure of $Sc_2W_3O_{12}$, where ScO_6 is blue and WO_4 is green [4] 24

Figure 5 – Representation of defects in a crystal lattice [24] 27

Figure 6 – Representation of a cationic substitution of a) A-site cation, and b) B-site cation [32] 30

Figure 7 – Representation of aliovalent substitution [31] 30

Figure 8 - Representation of oxygen vacancy formation through post-processing [31] 31

Figure 9 – Mass transport mechanisms leading to a) coarsening, b) densification, and c) neck formation [34] 33

Figure 10 – Schematic illustration of a pressure-less sintering method using an elevator furnace [12] 34

Figure 11 – Schematic representation of SPS system [36] 35

Figure 12 – Co-precipitation synthesis of $Al_2W_3O_{12}$ 42

Figure 13 – DSC/TG/DTG curves of the $Al_2W_3O_{12}$-based amorphous precursor from room temperature to 900 ºC. Exothermic peaks are oriented downwards. The dashed curve stands for DTG 45

Figure 14 – XRPD patterns of the as-prepared $Al_2W_3O_{12}$-based amorphous precursor and the powders calcined in air between 500 and 620 ºC. The diffraction peaks belonging to the orthorhombic phase are marked by a star symbol for the samples A510, A520, and A530 46

Figure 15 – DRS spectra of a) the as-prepared $Al_2W_3O_{12}$-based amorphous precursor and the powders calcined in air between 500 and 620 ºC, b) DRS spectrum of the powder calcined at 500 ºC illustrating two electronic transitions common for all calcined samples 49

Figure 16 – EPR spectra of the as-prepared $Al_2W_3O_{12}$-based amorphous precursor and the powders calcined in air between 500 and 620 ºC 51

Figure 17 – Raman spectra of the $Al_2W_3O_{12}$ powders calcined in air between 500 and 620 ºC within a) 100-1200 cm^{-1}, b) 800-1200 cm^{-1}, and c) Raman spectra of powders calcined in air between 500 and 620 ºC. The vertical dashed lines illustrate the red shift of the symmetric stretching vibrations with the decrease in calcination temperature. The vibration modes are marked by the bracket symbol 53

Figure 18 – XPS spectra of a) amorphous precursor, b) A620, and c) amorphous precursor and all calcined $Al_2W_3O_{12}$ powders 57

Figure 19 – a) XRPD patterns of the amorphous as-synthesized $Al_2W_3O_{12}$ powder and calcined milled and non-milled powders, and b) particle size distribution of amorphous as-synthesized $Al_2W_3O_{12}$ powder and calcined milled and non-milled $Al_2W_3O_{12}$ powders 65

Figure 20 – SEM of a) amorphous as-synthesized $Al_2W_3O_{12}$ powder, b) calcined non-milled $Al_2W_3O_{12}$ powder, and c) calcined milled $Al_2W_3O_{12}$ powder 66

Figure 21 – Dilatometric curves from a) high-temperature dilatometry, where shrinkage curves are represented by the dotted lines and their first derivative are represented by the solid lines, and b) SPS shrinkage curves 68

Figure 22 – XRPD patterns of the sintered $Al_2W_3O_{12}$ samples 70

Figure 23 – SEM micrographs of $Al_2W_3O_{12}$ sintered by a) RPLS sample R-m-10, b) SPS sample SPS-m-1000, and c) SPS pellet SPS-m-850 71

Figure 24 – Grain area distribution of the cross-section grain areas of the sintered bodies of $Al_2W_3O_{12}$ 73

Figure A1 – $Al_2W_3O_{12}$ powders from as-synthesized amorphous to calcined at 620 ºC 77

Figure A2 – Diffraction patterns of orthorhombic $Al_2W_3O_{12}$ powder calcined in air atmosphere at a) 540 ºC, b) 570 ºC, and c) 620 ºC 79

Figure A3 – TEM of the $Al_2W_3O_{12}$-based powders calcined at a) 500 ºC, b) 530 ºC, and c) 620 ºC 81

Figure A4 – Kulbeka-Munk of the $Al_2W_3O_{12}$-based powder calcined at 620 ºC 82

List of Tables

Table 1 – Sintering conditions and its respective densification, relative density, Vickers hardness, and Young's modulus 69

Table 2 – CTE measurements in the direction of the applied pressure (z-axis), and along the direction perpendicular to the applied pressure (x and y axes) 74

Table A1 – Unit-cell volumes of the samples A540, A570, and A620 81

Table A2 – SETOV concentration of the amorphous powder and the powders calcined from 500 ºC to 620 ºC 82

1 Introduction

When submitted to heat, most solid materials expand, a process known as positive thermal expansion. However, a class of materials recently denominated as thermomiotic do not present the same behavior, i.e., contracting upon heating. These material's coefficient of thermal expansion (CTE) ranges from low positive, and negative, to near zero [1,2].

Most tungstates and molybdates belonging to the $A_2M_3O_{12}$ family of materials, where A is a trivalent cation of Al, Y, Sc, etc., have been a recurrent topic of study due to their vast chemical flexibility and tunable low positive to near-zero CTE [1,3–7]. These features allow many potential applications such as high-precision optical devices [8]. In addition, a possible mechanism for tunning the CTE might be the introduction of extrinsic oxygen vacancies into their garnet-deficient crystal structure [9].

Meanwhile, the vast chemical flexibility and the tunable CTE suggest that the $A_2M_3O_{12}$-type materials can be used, among other things, for thermal shock resistance applications [10,11]. Advanced sintering techniques often require a deagglomerated fine powder to produce fully dense samples, [12] which is still a challenge due to the nature of a nanometric powder. Pressure-less sintering techniques provide a low cost and, usually, longer production, not allowing good control over the microstructure. Pressure-less or conventional sintering can achieve densities as high as those obtained by pressure-assisted methods, however at the cost of longer periods and secondary or tertiary stages. Pressure-aided sintering methods, such as SPS and HIP, provide better odds of fully densifying ceramics in relatively shorter periods with even lower temperature ranges. Although SPS sintering is quite promising, producing highly dense ceramics with controlled microstructure and microcrack-free remains a challenge. In addition, studies that compare different sintering techniques of the $A_2M_3O_{12}$ family on the densification and microstructure evolution are still lacking.

Among $A_2M_3O_{12}$-type materials, $Al_2W_3O_{12}$ was chosen due to its low cost and easy production, being a good candidate for applications that require low thermal expansion. However, the major challenge is to produce a fully dense ceramic with fine microstructure and low CTE. A few oxides from the $A_2M_3O_{12}$ family have been studied for this purpose, such as $Al_2W_3O_{12}$ by Prisco et al. [10], and $Al_{0.5}Sc_{1.5}W_3O_{12}$ by Dasgupta et al. [8], both showing promising results for applications such as transparent infra-red (IR) windows.

Based on these features this work is divided into two aspects. The first aims on the evaluation of the influence of oxygen vacancies in the crystallization of $Al_2W_3O_{12}$ during the calcination process in ambient air. The second aspect aims on the comparative study of different sintering techniques (RPLS and SPS) using both milled and non-milled powders of $Al_2W_3O_{12}$, and its influence on microstructure, densification, and mechanical properties.

2
Literature Review

2.1
Thermal Expansion

In general, most solids expand when heated, a behavior known as positive thermal expansion, (PTE) [2,3] and can be explained through the curve of potential energy as a function of interatomic distance. Few materials are known to contract on heating, which is a behavior known as negative thermal expansion (NTE).

Solids with positive CTE expand, macroscopically increasing its dimension and volume, due to, overall, an increase in the interatomic bond length upon heating. Figure 1 represents the potential energy (E) versus interatomic distance (r) curve and shows that the slope of the potential energy curve is higher for shorter interatomic distances. Therefore, due to the well asymmetry, the mean interatomic distance tends to increase with temperature as the vibrational energy increases. Accordingly, materials with stronger interatomic bonds results in deeper, and narrower potential wells, which leads in a smaller CTE due to the slower rate of increase of interatomic distance [2,3].

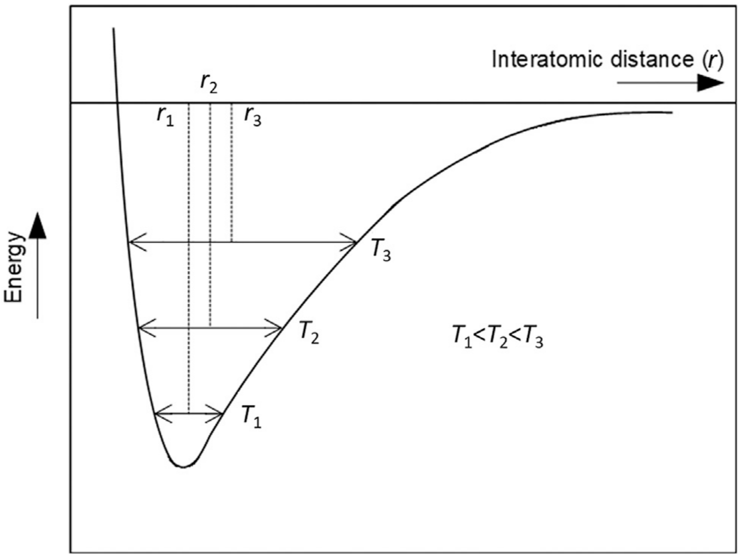

Figure 1: Diagram of an asymmetric potential energy well. [1]

In addition, the asymmetry of the potential energy well is responsible for PTE behavior. While in NTE materials, the potential energy curve is not sufficient to explain this phenomenon since NTE generally arises from supramolecular mechanisms such as phase transformation and low frequency phonon modes [2,13]

2.1.1

Coefficient of Thermal Expansion - CTE

The CTE can be explained as a measure of the volumetric (or linear) change by the temperature, as defined by equation 1 and 2 [2].

$$\alpha_v = \frac{\Delta V}{V_0 \Delta T} \tag{1}$$

α_v *is the volumetric coeficient of thermal expansion*
ΔV *is the volumetric change*
V_0 *is the inital volume*
ΔT *is the temperature change*

$$\alpha_l = \frac{\Delta l}{l_0 \Delta T} \tag{2}$$

α_l *is the linear coeficient of thermal expansion*
Δl *is the length change*
l_0 *is the inital length*
ΔT *is the temperature change*

In isotropic solids, thermal expansion can be described as a function of both equations, as described by equation 3.

$$\alpha_v = 3\alpha_l \tag{3}$$

Anisotropic solids do not follow the same behavior therefore the linear CTE can’t be measured directly by the previous equations, therefore the CTE should be evaluated in all crystallographic directions separately. In anisotropic solids, the crystallites have different orientations within the crystal structure, therefore each crystal axis can present different CTE values. This behavior can lead to microcracking during the sintering process of ceramics [2,14].

In addition, the compaction of a fine powder can lead to different orientations of the crystallites when packing, which can magnify an already anisotropic NTE in one axis.[2] On the cooling process, after sintering, the crystals contract unevenly, giving rise to inner tensions that when exceed locally the mechanical resistance of the material, results in microcracks [2,14]. The formation of microcracks on polycrystalline anisotropic solids, specially at the grain boundaries, can directly affect thermal and mechanical properties, such as thermal expansion and modulus of elasticity. This feature remains an issue for the production of highly density ceramics since it can prevent full densification, also affecting the integrity of the bulk material. However, since the formation of microcracks is strongly dependent on grain size, larger grains, that exceed the critical size for certain stress magnitude, will start microcrack propagation, while smaller grains will not [15,16] Therefore, ceramics with finer microstructure are more likely to produce highly dense bodies.

2.1.2

Negative Thermal Expansion

There are many mechanisms responsible for NTE in solids, however, the majority of the structures with reported NTE have a M-O-M linkage (metal-oxygen-metal) which are responsible for NTE behavior. A quantized vibrational mode is often a phonon, in which the most important low frequency phonon modes are longitudinal and transverse vibrations, as shown in Figure 2 [2,3]. It seems that these modes are responsible for NTE behavior in many open framework structures.

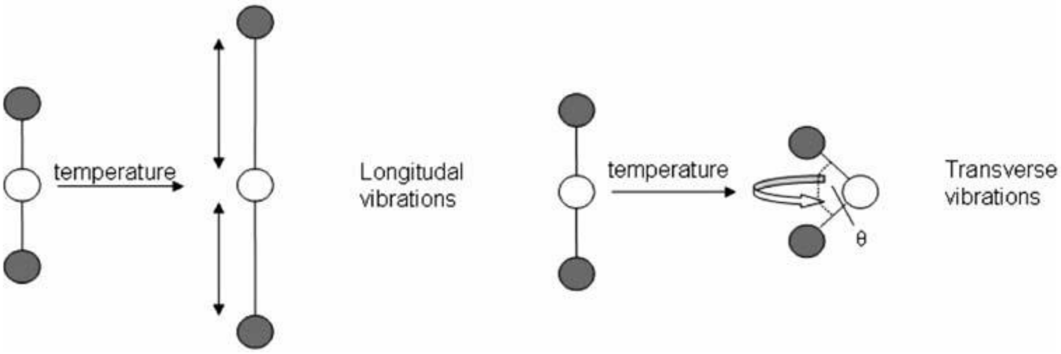

Figure 2: Longitudinal and transverse vibrations of M-O-M links. [2]

Longitudinal vibrations alternate between compression and expansion of the M-O-M links as depicted in Figure 2. For this reason, and due to the asymmetric nature of the potential energy curve, the result is PTE. The longitudinal vibrational modes tend to increase M-O bond length upon heating, as well as M···M interatomic distances. In contrast, the opposite effect happens in transverse vibrational modes, reducing M···M distances due to changes in M-O-M angle. These changes in angle are caused by an amplitude increase of the oxygen atom's vibration [2].

Most oxides structures are composed by an open framework of rigid or quasi-rigid corner-linked polyhedra (tetrahedra and/or octahedra), which are free to rotate, forming M-O-M linkages. Unlike other structures, the polyhedra are more rigid, thus having higher frequency phonon modes known as rigid unit modes (RUMs) [2]. In these structures, the polyhedra are subjected to bending or rotation, as well as distortion [2,17]. As explained previously, the transverse vibrational modes cause a reduction in M···M distances within M-O-M links, resulting in NTE, as shown in Figure 3 [2].

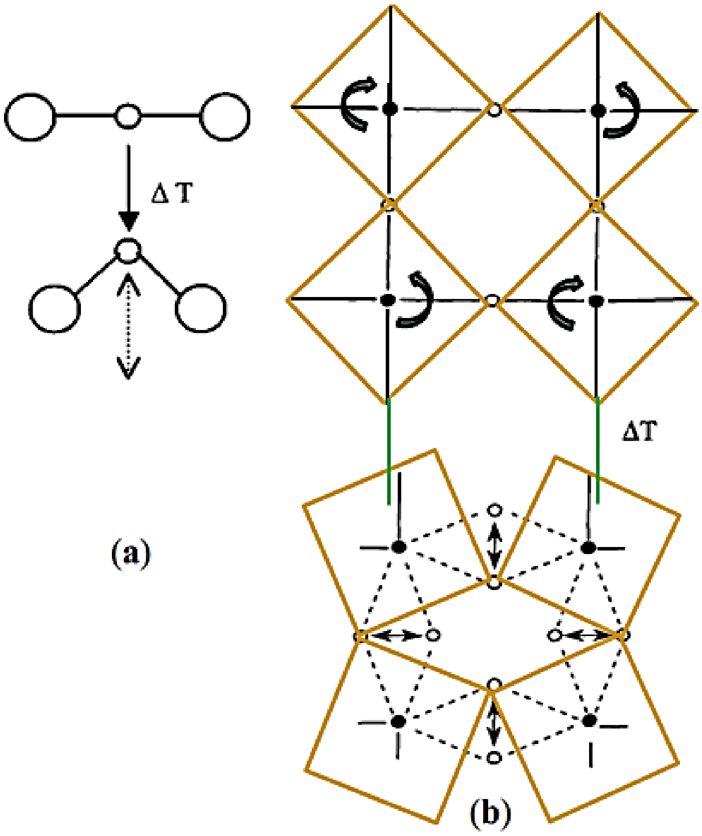

Figure 3: Schematic representation of a) transverse vibrational modes of M-O-M links, and b) rotation mechanism of polyhedra. [17]

$A_2M_3O_{12}$-type structures can alter NTE, among other mechanisms, by changing cations into A position of the octahedra. Increasing the size of the cation

A can increase the NTE effect due to the increase in oxygen-oxygen (anion-anion) distances. This process results in a decrease in oxygen repulsion, thus decreasing the rigidity of the polyhedra, and generation distortions. In addition, there must be slight distortions of the polyhedra for rotation to occur, and therefore affect the NTE effect [2].

2.2

$A_2M_3O_{12}$ family

$A_2M_3O_{12}$-type materials are widely studied due to their outstanding chemical flexibility, tunable low positive, negative, to near-zero coefficients of thermal expansion, and vast potential applicability from cooker hobs to housing for optical devices. Among the mechanisms for tuning their CTE are the substitution of the A^{3+} cation, the insertion of bulky molecules inside the nanochannels of their crystal structure, and, possibly, the formation of extrinsic oxygen vacancies.[1]

Multiple materials from this family present anisotropic CTE, i.e., displaying NTE along one or more axes, thus resulting in a range of materials with low positive, negative, and near-zero CTE [1]. Their structure consists of an open framework of corner-sharing AO_6 octahedra and MO_4 tetrahedra, as shown in Figure 4 for $Sc_2W_3O_{12}$, forming A-O-M and M-O-M linkages [2]. In the monoclinic configuration, the materials usually present anisotropic PTE, while in orthorhombic configuration this behavior is affected by the cation size, where larger A cations can reduce NTE value. Such anisotropy in polycrystalline materials with randomly oriented grains can lead to microcracks of sintered bodies due to thermal stresses during the heating cycle [18].

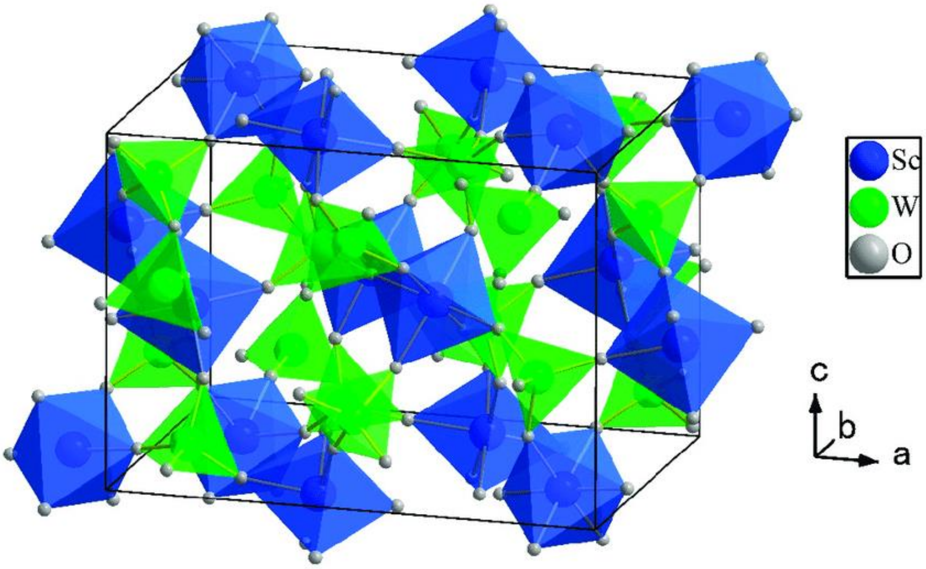

Figure 4: Orthorhombic crystal structure of $Sc_2W_3O_{12}$, where ScO_6 is blue, and WO_4 is green. [4]

This feature makes $A_2M_3O_{12}$-type materials great candidates for applications that require thermal shock resistance despite the microcracking formation. Additionally, extrinsic point defects, such as oxygen vacancies, seem to be a tool for tailoring the CTE, as reported by Cheng et al., [6] who introduced the oxygen vacancies into $In_{0.6}(HfMg)_{0.7}Mo_3O_{12}$ phase (belonging to $A_2M_3O_{12}$-family by heat treatment in He atmosphere. The oxygen vacancies enhanced the negative CTE when compared to the extrinsic defect-free material calcined in air, from -0.47×10^{-6} to -1.5×10^{-6} K^{-1}, between 323 and 573 K.

2.2.1
Synthesis of $A_2M_3O_{12}$ materials

$A_2M_3O_{12}$-type materials can be synthesized through various methods, such as solid-state reaction, sol-gel, hydrothermal method, and co-precipitation [19–24]. The most conventional route is the solid-state reaction, however, although this method does not require sophisticated chemistry, this synthesis often produces inhomogeneous submicronic powder, with large, agglomerated particles, and can produce secondary phases, which is a problem when producing highly dense ceramics with fine microstructure. Meanwhile, soft-chemistry routes, such as co-precipitation synthesis, can produce submicronic to nanometric powder with less agglomeration than other methods.

2.2.1.1
Co-precipitation principles

The co-precipitation synthesis is a simple soft-chemistry route that allows the production of nanometric powders. In this process, usually, an aqueous solution of metal salts is mixed with aqueous solutions of a precipitation agent forming supersaturated solutions, thus involving three main steps: embryo/nucleus formation, nucleation, and growth. The interaction between molecules and ions in the solution forms embryos that can grow until it reaches a critical size (r*). Critical size can be described as an intermediate size at which the system's free energy decreases independently of the nucleus dissolution or growth. Small embryos, smaller than the critical radius, are unstable and it most likely dissolve rather than grow. Therefore, the nucleus of radius equal to or higher than the critical size can surpass the activation energy, giving rise to nucleation and consequential growth. However, if the solution's supersaturation is sufficiently high, the critical size can be reduced [25,26].

The equation 4 describes the activation energy, which is inversely related to the supersaturation level.

$$\Delta G^* = \frac{16\pi v^2 \gamma^2}{3(kT)^2(lnS)^2} \tag{4}$$

ΔG^* *is the Gibbs free energy of the system*

v *is the molecular volume of the solute*

γ *is the interfacial energy between the solute and the solution*

k *is the Boltzmann's constant*

T *is the temperature in Kelvin*

S *is the supersaturation level*

The supersaturation level is defined by the equation 5.

$$S = \frac{C}{C_S} \tag{5}$$

$S \text{ is the supersaturation level}$

$C \text{ is the solute concentration}$

$C_S \text{ is the saturation concentration}$

In addition, the nucleation rate can be described by the equation 6 bellow.

$$J = J_0 \exp\left[\frac{16\pi v^2\gamma^2}{3(kT)^2(lnS)^2}\right] \tag{6}$$

$J \text{ is the nucleation rate}$

$J_0 \text{ is the rate constant}$

The growth rate is defined by equation 7.

$$K_g = a(C - C_s)^b \sim aS \tag{7}$$

$K_g \text{ is the Growth rate}$

$a \text{ is the growth's constant}$

$C \text{ is the solute concentration}$

$C_S \text{ is the saturation concentration}$

Therefore, as described by the equations above, the nucleation rate increases with the supersaturation level. A high nucleation rate can lead to the formation of multiple smaller particles rather than growth [25].

2.3
Point defects in ceramics

Ceramic materials present a large range of defects that play an essential role in chemical and physical properties of materials. Defects can be classified into dimensionality:

1. Zero-dimensional – point defects (vacancies)
2. One-dimensional – linear defects (dislocations)
3. Two-dimensional – planar defects (surfaces and grain boundaries)

4. Three-dimensional – volume defects (precipitates)

Defects are commonly associated with crystalline materials due to periodicity of the crystal structure, where atoms are arranged in regular repetition, therefore a disturbance in the periodicity of the crystal lattice constitutes a defect [27]. Amorphous materials are harder to define a defect since they lack long-range order as crystalline materials do, however, the structure of amorphous ceramics, such as glass, are not random, therefore they too can have defects [28]. Unlike metals, point defects in ceramics can carry charge, providing a whole range of various effects, and applications, such as the color of different precious gems, otherwise colorless, due to an electron trapped in a vacancy (F centers), or alter the band gaps in different semiconductors and insulators.

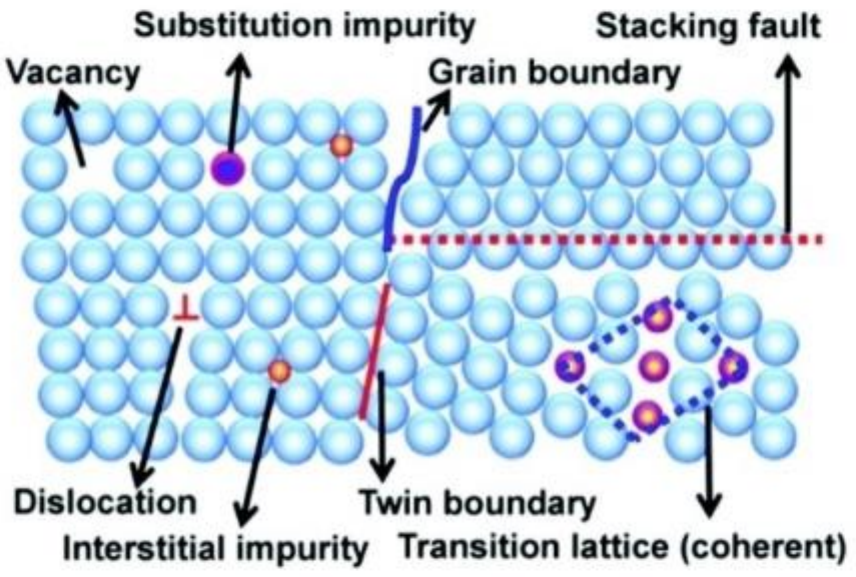

Figure 5: Representation of defects in a crystal lattice. [29]

Point defects are localized defects classified as 0-dimensional, and can be intrinsic, coming from the material itself, such as vacancies, or extrinsic, from an external source, such as impurities. Vacancies are the simplest point defects and can be defined as any atomic position that is not occupied by either an atom or ion that otherwise is necessary to maintain the periodicity of the crystal structure.

In sintered ceramics, the presence of voids and pores have negative effects on the production of highly dense ceramics because they prevent full densification of the material, while also weakening it. In addition, for transparent ceramics, voids and pores are problematic due to light scattering effect. However, porous ceramics is of interest for other applications, such as catalysts and semiconductors, since it usually present high surface area and allows fine-tuning of physical properties [28].

2.3.1

Point defects notation for ionic compounds

The Kröger-Vink notation, described in equation 8, is usually used when describing point defects in crystal structures because it can describe any point defect while considering charge neutrality and mass balance.

$$X_Y^Z \tag{8}$$

$X\ is\ what\ is\ situated\ in\ the\ site$

$Y\ is\ the\ type\ of\ crystal\ site\ that\ is\ occupied\ by\ X$

$Z\ is\ the\ relative\ charge\ of\ the\ defect$

If a vacancy is on the site, X turns into V (for a vacancy), and if it is an element, it becomes the elemental notation (e.g. Al). Y can stand for different types of sites, such as i for interstitial, or l for lattice. Positive charges are represented by a dot (˙ or ¨), and negative charges are represented by primes ($'$ or $''$) however, a neutral (zero) charge can be represented by an x [30]. Therefore, cation vacancies carry a negative charge while anion vacancies carry positive charge.

Oxygen vacancies can be described by the Kröger-Vink notation, as shown in equation 9.

$$O_O^x \rightarrow \frac{1}{2} O_2(g) + V_O^{\cdot\cdot} + 2e' \tag{9}$$

It can be seen by the equation above that the left side of the reaction an atom of oxygen (O) is situated at the oxygen site (o) and has neutral charge (x). The right side of the equation shows that the oxygen is in the gaseous state (g), forming a vacancy ($V_O^{\cdot\cdot}$) with two positive charges (¨), thus, to maintain charge neutrality two electrons (negative charge $'$) are needed (e) [28].

The Kröger-Vink notation can also be used for ionic point defects, such as Schottky and Frenkel defects, as shown in the equations 10 and 11, respectively. Shottky defects arise from a balanced number of cation and anion vacancies in a crystal. While Frenkel defects consists of a displacement of an atom or ion from its original position into the interstice forming a vacancy.

$$null = V_x^{\cdot} + V_M' \tag{10}$$

$$M_M = M_i^{\cdot} + V_M' \tag{11}$$

In the Shottky defect, $null$ is used to represent the defect-free lattice, thus forming a vacancy with positive charge in site x ($V_x^{\cdot}$), and a vacancy negatively charged in site M (V_M'), i.e., a pair of cation and anion vacancies. In the Frenkel defect an M atom on M site (M_M), forms a positively charged M ion located at the interstitial site ($M_i^{\cdot}$), and a vacancy at M site with negative charge (V_M') [30].

Materials with low coordination number and open lattice usually prefers Frenkel defects, while materials with high coordination number (> 6) tend to have Shottky defects. This happens because crystals that do not have much space in its lattice cannot accept an interstitial atom. $Al_2W_3O_{12}$, member of the $A_2M_3O_{12}$ family, with a 6-fold coordination has a Shottky defects as described in equation 12 bellow.

$$null \rightarrow 2V_{Al}''' + 3V_W'''''' + 12V_O^{\cdot\cdot} \tag{12}$$

2.3.2
Oxygen vacancy formation

There are many ways of producing oxygen vacancies in ceramic compounds, such as irradiation, formation in crystallization/crystal growth, or through post-treatments, like heat treatment in a reducing or oxidizing atmosphere of an already crystalline material. In sintered materials, oxygen vacancies can be generated by applied pressure while in oxygen atmosphere.

In cation substitution, a lower valence cation is substitute in the place of a cation upsetting charge neutrality, therefore, an oxygen vacancy of balanced charge is formed, as shown in Figure 6. Additionally, cation substitution in the A site tends to form oxygen vacancies, while cation substitution in the B site tends to change the electronic structure without forming oxygen vacancies [31,32].

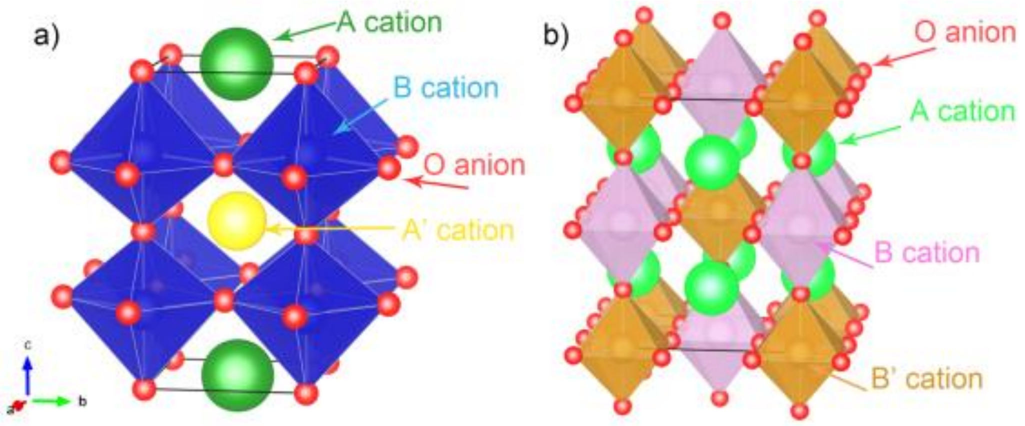

Figure 6: Representation of a cationic substitution of a) A-site cation, and b) B-site cation. [32]

In aliovalent substitution an ion of a determined valence is substituted by an ion of a different valence, creating a charged defect (vacancy), as shown in Figure 7. In the figure below it can be seen that an oxygen vacancy is formed, to maintain charge neutrality disturbed by the partial substitution of A ion, through the release of oxygen from the lattice. This feature happens through ionic compensation, where a vacancy or interstitial atom carrying a balanced charge is introduced to maintain charge neutrality.

In isovalent substitution, a partial substitution of A atoms by another valance atom also occurs. However, unlike aliovalent substitution, ionic charge compensation does not occur. A distortion of the structure is responsible for the oxygen vacancy formation, also forming electrons or holes. This compensation is known as electronic compensation.

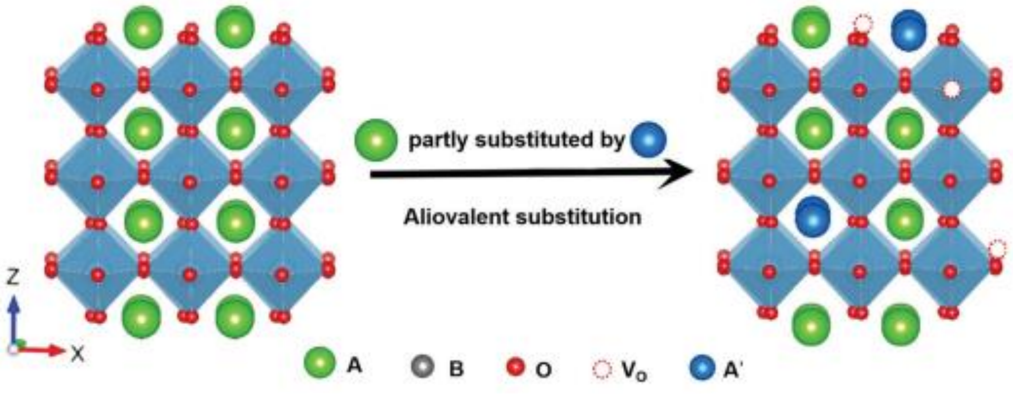

Figure 7: Representation of aliovalent substitution. [31]

Non-stoichiometry anions can also be used to generate oxygen vacancies. It usually happens in post-processing techniques, when the material is heat treated in oxidizing or reducing atmospheres, in processes such as annealing [31]. Figure 8 shows that the oxygens from the lattice, of the perovskite structure, can move to the surface forming oxygen vacancies.

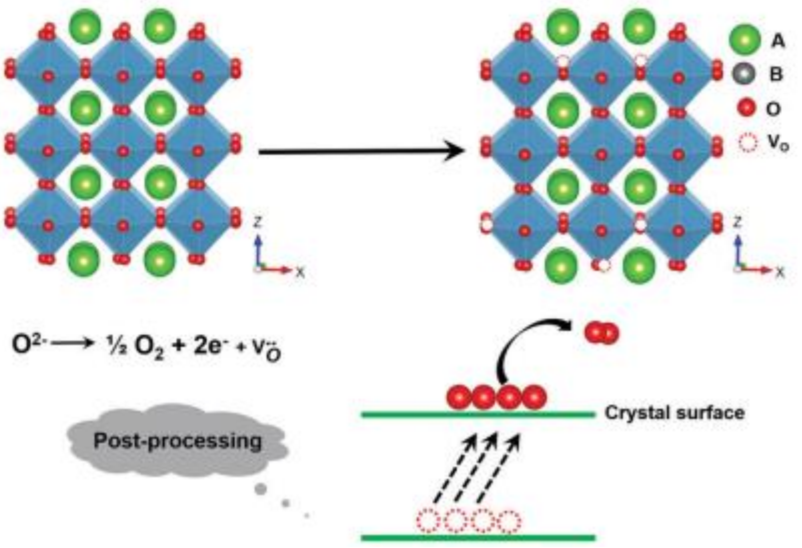

Figure 8: Representation of oxygen vacancy formation through post-processing. [31]

In addition, point defects are more mobile than extended defects so they can order themselves at low temperatures and disorder at high temperatures [27]. Therefore when a material is ordering itself, point defects such as oxygen vacancies can be assimilated into the crystalline structure or vanish [27].

2.4
Sintering

The production of highly dense ceramics with suitable mechanical and physical properties relies on the production of homogeneous and fine microstructure, where the grains do not exceed the critical size for microcrack propagation. Starting powders with submicronic to nanometric size and low agglomeration can lead to a finer and more homogeneous microstructure, which, in turn, can increase densification.

Consolidation and subsequent sintering techniques have a great impact on the microstructure, mechanical and physical properties of bulk ceramics materials.

Many applications require highly dense materials, such as optical transparency devices [8].

Sintering is the process by which a powder is transformed into a solid by thermal treatment at temperatures lower than its fusion point. Many techniques require prior consolidation to produce compact bodies, known as green bodies, to either mold them into a specific shape or because the technique does not allow sintering for loose powder.

The compression of the starting powder can be done with uniaxial or isostatic pressing. In uniaxial pressing, the powder is poured into a mold and pressed unilaterally to form a compact pellet. In isostatic pressing, the pellet is further pressed while submerged in a liquid, allowing it to be pressed evenly at all directions [33]. This process considerably reduces the non-uniformity of the outside of the pellet in uniaxial pressing due to wall friction.

The sintering process is dictated by mass transport, in which its driving force is the reduction of superficial energy. These atoms diffusion process either lead to densification, through mass transport from inside the grains into the pores or it can lead to coarsening of the microstructure by the rearrangement of matter causing grain growth without pore reduction, as shown in Figure 9.

Among the densification mechanisms are:

1. Lattice diffusion: from bulk to the neck, depicted as path 5 in Figure 9
2. Grain boundary diffusion: from the grain boundary to the neck, depicted as path 4 in Figure 9
3. Plastic deformation: dislocation to the neck region

While the coarsening mechanisms are:

1. Surface diffusion: from the surface to the neck, depicted as path 2 in Figure 9
2. Evaporation/Condensation: from the surface to the neck, shown as path 1 in Figure 9
3. Lattice diffusion from grain boundary: from the surface to the neck area, or path 3 in Figure 9

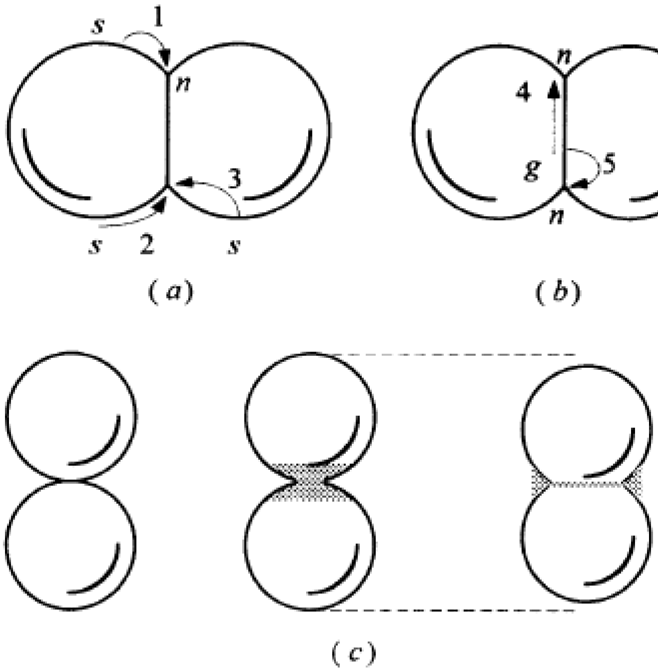

Figure 9: Mass transport mechanisms, leading to a) coarsening, b) densification, and c) neck formation. [34]

As shown in Figure 9, the coarsening mechanisms cause mass to move from the convex surface to the concave surface. This process causes a change in neck size and pore geometry, and it can cause coalescence, which is the growth of bigger grains at the expense of smaller ones without causing densification. In contrast, the densification mechanism is processes that lead to sintering.

2.4.1
Rapid Pressure-less Sintering - RPLS

Conventional sintering is the most common sintering method to mass-produce ceramics of various shapes [12]. However, conventional sintering usually requires a longer time and a slower heating rate. Rapid Pressure-less sintering (RPLS) is the sintering of a material without the aid of pressure, i.e., under atmospheric pressure, as conventional sintering, and it can be performed in a resistive furnace as conventional sintering. Figure 10 shows the scheme of this system that was performed in an elevator furnace. Unlike conventional sintering, the RPLS allows shorter holding time and faster heating heat, reaching even higher densities.

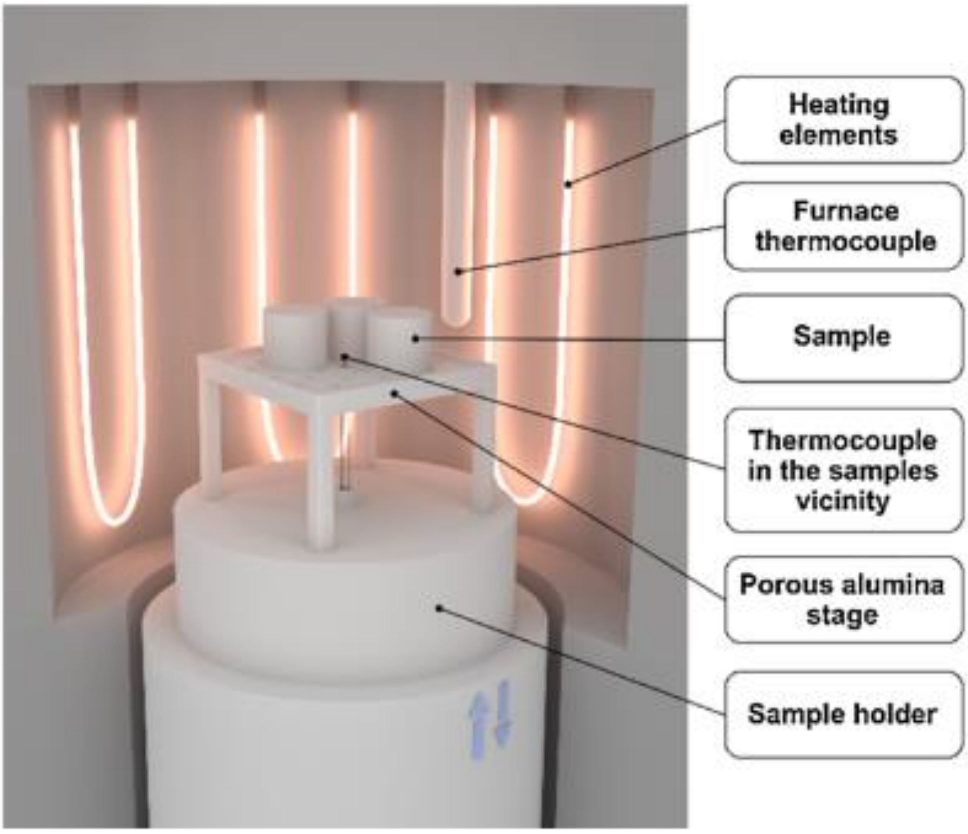

Figure 10: Schematic illustration of a pressure-less sintering method using an elevator furnace. [12]

RPLS can have a few setbacks preventing full densification of ceramics. The temperature is higher in the surface of the material due to the contribution of convection to the irradiation heat transfer process; therefore, the densification occurs faster in the surface forming a nearly dense shell that prevent further shrinkage and consequential densification [12]. In addition, although the microstructure obtained in RPLS is finer than the one obtained by conventional sintering, a non-homogeneous microstructure can occur due to an uneven densification [35]. This feature can be an artifact produced by a non-homogeneous starting powder or due to the shell formation.

2.4.2
Spark Plasma Sintering - SPS

Spark Plasma Sintering (SPS) uses uniaxial pressure along with pulsed electrical current. It is similar to other pressure-assisted methods such as hot pressing and hot isostatic pressing, where the powder is placed into a graphite die and heated through resistive heating. However, in SPS there is also a direct electrical pulse, which forms a plasma [35].

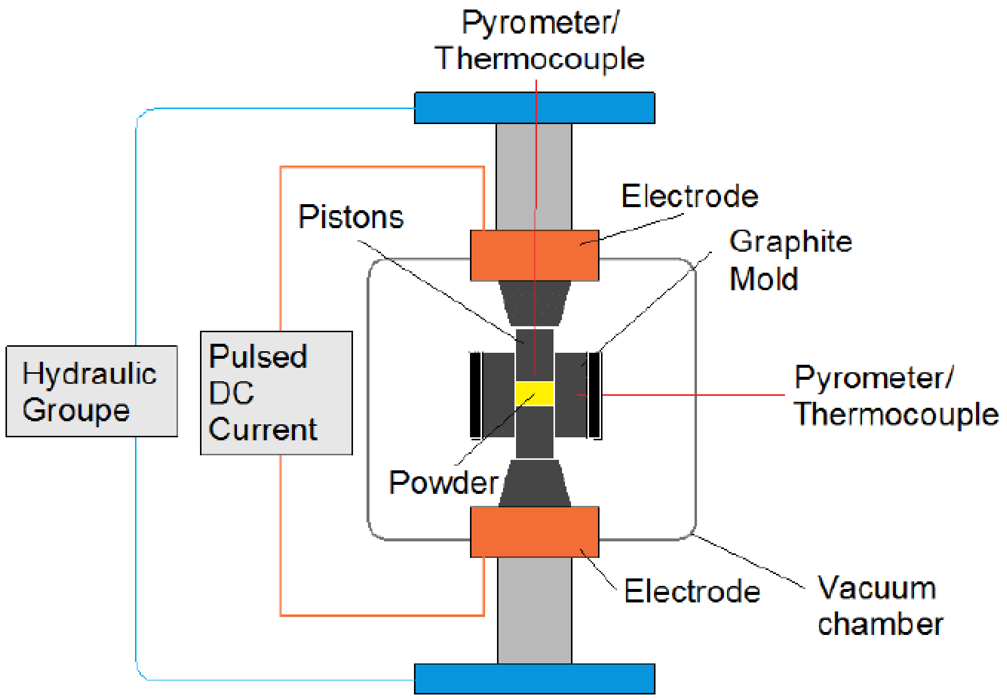

Figure 11: Schematic representation of SPS system. [36]

The heating mechanism has a low-voltage high-intensity current that flows directly through the die and into the sample, i.e., the sample is heated through Joule heating. This feature allows high heating rates due to the dieletric breakdown [35,37]. It is speculated that the fast-heating rates and intense electrical pulses are responsible for spark discharges that are generated in the voids between particles, forming a localized plasma. This localized plasma enhanced the diffusion process on the surface of the powder helping densification [38].

The densification mechanisms in pressure-assisted methods are dictated by pressure. Besides lattice diffusion and grain boundary diffusion, there is plastic deformation which is unimportant for pressure-less techniques [35]. Firstly, an electrical discharge heats the surface of the particles evenly, where they organize, and then pressure is applied which causes plastic deformation and further densification. Applied pressure at the sintering temperature speeds the densification process due to the constant contact between particles and rearrangement of particles, improving packing and therefore consolidation. This feature allows shorter holding times and lower temperatures, achieving higher densifications than the pressure-less methods with finer microstructure [39,40].

3
Objectives

3.1
General objectives

3.1.1
General objectives of the first scope

Introduce oxygen vacancies into $Al_2W_3O_{12}$ through the calcination in air at varying temperatures.

3.1.2
General objectives of the second scope

Produce $Al_2W_3O_{12}$ ceramics with densities higher than 99 % of the theoretical density (TD) to the production of infrared transparent windows.

3.2
Specific objectives

3.2.1
Specific objectives of the first scope

Evaluate the influence of the oxygen vacancies on the crystallization process during calcination in air.

3.2.2
Specific objectives of the second scope

1. Produce submicronic to nanometric powders of $Al_2W_3O_{12}$ via co-precipitation.

2. Evaluate the evolution of densification and microstructure through different sintering techniques: RLPS and SPS.

4

Extrinsic oxygen vacancies formation during crystallization of $Al_2W_3O_{12}$ by calcination in air

4.1

Introduction

Aluminium tungstate is a wide-band-gap semiconductor belonging to the family of mostly tungstates and molybdates with the general chemical formula $A_2M_3O_{12}$, where A = Al^{3+}, Y^{3+}, Sc^{3+}, Ho^{3+}, etc., and M = W^{6+} or Mo^{6+}. Many $A_2M_3O_{12}$-type materials have been a recurrent topic of studies due to their vast chemical flexibility since almost 20 different, predominantly, trivalent cations could enter the A position, and 5 different hexavalent or pentavalent cations fit into the M position without modifying their garnet-deficient crystal structure [1]. This feature provides a large range of compounds with a tunable coefficient of thermal expansion (CTE) and unusual physical and chemical properties [1,3–8,10,11,41–43]. $Al_2W_3O_{12}$ adopts an orthorhombic structure at room temperature (Pbcn space group) consisting of an open framework of corner-sharing AlO_6 octahedra and WO_4 tetrahedra [1]. In addition, the formation of extrinsic oxygen vacancies in this family seems to add extra lattice flexibility, permitting finetuning of CTE, [9] and might corroborate the average atomic volume model, recently extended and proposed for anisotropic materials [44].

Point defects play an essential role in the physical properties of materials, influencing a wide range of applications such as thermal and chemical sensors, optical devices, and transparent infrared windows [8,45–47]. In semiconductors and insulators, these defects can affect electrical, thermal, optical, and photochemical properties by modifying the band gap energy and, hence, its radiation absorption, by forming intermediate energy states within the band gap [9,45,46]. TiO_2 nanofibers [48] showed a formation of oxygen vacancies when heat-treated in 100% Ar atmosphere, significantly lowering the optical band gap from 3.33 to 2.18 eV. $MgFe_2O_4$ [49] photocatalysts calcined in air displayed, on the other hand, an increase of the band gap as the calcination temperature and oxygen vacancies concentration increased, going from 1.99 eV at 650 °C to 2.17 eV at 750 °C. $Al_2W_3O_{12}$ [9] heat-treated in Ar and H_2 atmospheres, respectively, lowered the optical band gap when oxygen vacancies were introduced, changing it from 3.26 to 2.29 eV, respectively. Therefore, the as-prepared materials presented a greater absorption within the visible spectrum than the extrinsic defect-free counterpart. Many other oxides have been studied for extrinsic point defects due to their influence on thermal properties. Oxygen vacancies can be used to reduce the thermal conductivity of oxides, as demonstrated for $La_2Mo_3O_{12}$ [50], $Zr_3Ln_4O_{12}$ [51], and ZnO, [52] due to the phonon scattering effect. $La_2Mo_3O_{12}$ [50], a scheelite-type oxide, showed a very low thermal conductivity of 0.59 Wm^{-1} K^{-1} after the introduction of extrinsic oxygen vacancies. The compounds of $Zr_3Ln_4O_{12}$ [51] (Ln = La, Gd, Y, Er, and Yb) and ZnO [52] also showed low thermal conductivities of 1.3−1.6 and 3.05 Wm^{-1} K^{-1}, respectively, after the introduction of oxygen vacancies.

Additionally, extrinsic point defects, such as oxygen vacancies, seem to be a tool for tailoring the CTE, as reported by Li et al. for $Sm_{1-x}Cu_xMnO_{3-\delta}$ [53], where the thermal expansion reduction was attributed to oxygen vacancies and pore formation in the sintered body. Li et al. found that the linear CTE of $Sm_{0.85}Cu_{0.15}MnO_{3-\delta}$ sintered in air decreased from 5.24×10^{-6} to -5.93×10^{-6} K^{-1} between 473 and 873 K, when compared to the undoped $SmMnO_3$. A similar feature was reported by Zhang et al. for $HfMnMo_2PO_{12-\delta}$ [7], where the extrinsic oxygen vacancies affected the linear CTE (-3.59×10^{-6} K^{-1}) between room temperature and 420 K. The essential results for our study were published recently by Cheng et al., who introduced the oxygen vacancies into $In_{0.6}(HfMg)_{0.7}Mo_3O_{12}$ phase (belonging to $A_2M_3O_{12}$-family) [6] by heat treatment in He atmosphere. The oxygen vacancies enhanced the negative CTE when compared to the extrinsic defect-free material calcined in air, from -0.47×10^{-6} to -1.5×10^{-6} K^{-1}, between 323 and 573 K. More recently, Moreno Diaz et al. found that $Al_2W_3O_{12}$ [9] showed a lowering of about 33 and 40% in the linear CTE when oxygen vacancies were introduced through heat treatment in Ar or H_2, respectively, of previously well-crystallized $Al_2W_3O_{12}$, in comparison to the extrinsic defect-free phase. Therefore, the oxygen-defective $Al_2W_3O_{11.36}$ phase, obtained by heating in the H_2 atmosphere, presented a near-zero thermal expansion with a CTE of 0.90×10^{-6} K^{-1} from room temperature to 673 K.

A survey of the literature shows that multiple studies approached the crystallization of different ceramic phases through calcination, including $Al_{2-\delta}Sc_{\delta}W_3O_{12}$ [54], $Al_2W_3O_{12}$ [9,55], $Sc_2W_3O_{12}$ [55], $Cr_{2x}Fe_{2-2x}Mo_3O_{12}$ [54], $Al_{2x}Cr_{2-2x}Mo_3O_{12}$ [54], $Al_{2x}Fe_{2-2x}Mo_3O_{12}$ [54], $BaMoO_4$ [50], $La_2Mo_3O_{12}$ [50], TiO_2 [56,57], and Ga_2O_3 [58]. However, to the best of the author's knowledge, no efforts have been made to understand the mechanism of crystallization from amorphous powder and its relation to the introduction of extrinsic oxygen vacancies through calcination in air, especially within the $A_2M_3O_{12}$ family. Although Fu et al. found that $MgFe_2O_4$ [49] presents a direct relationship between the heat treatment temperature and the formation of oxygen vacancies, the study was conducted, from 650 to 850 °C, using the already crystalline material.

The present study aims to understand the formation and evolution of extrinsic point defects during the crystallization of orthorhombic $Al_2W_3O_{12}$ starting from an amorphous powder prepared by co-precipitation, through calcination at different temperatures in the air atmosphere.

$Al_2W_3O_{12}$ was chosen among the phases of the $A_2M_3O_{12}$ family due to its low cost and facile synthesis. The amorphous powder was calcined for crystallization in air at temperatures between 500 and 620 °C. The amorphous powder was used as a reference material for comparison with the calcined samples. The crystallization temperature and the mass losses were investigated with differential scanning calorimetry (DSC) and thermogravimetry (TG). The phase composition was studied by X-ray powder diffraction (XRPD), while the unit-cell parameters were evaluated by the Pawley method. The formation of the oxygen vacancies and their effect on charge compensation was evaluated by electron paramagnetic resonance (EPR), Raman spectroscopy, and X-ray photoelectron spectroscopy (XPS). The absorption spectra were acquired by diffuse reflectance spectroscopy (DRS), and the band gap energy was evaluated by the Kubelka−Munk plot.

4.2
Materials and Methods

4.2.1
Synthesis of $Al_2W_3O_{12}$

$Al_2W_3O_{12}$-based amorphous powder was prepared by the co-precipitation method. $Al(NO_3)_3$ $9H_2O$ (Alfa Aesar) and Na_2WO_4 $2H_2O$ (Sigma-Aldrich) were used as precursors without additional purification. In accordance with the stoichiometric ratio of 2:3, these were dissolved in distilled water at room temperature to form 0.005 M solutions of the reagents, as shown in Figure 12.

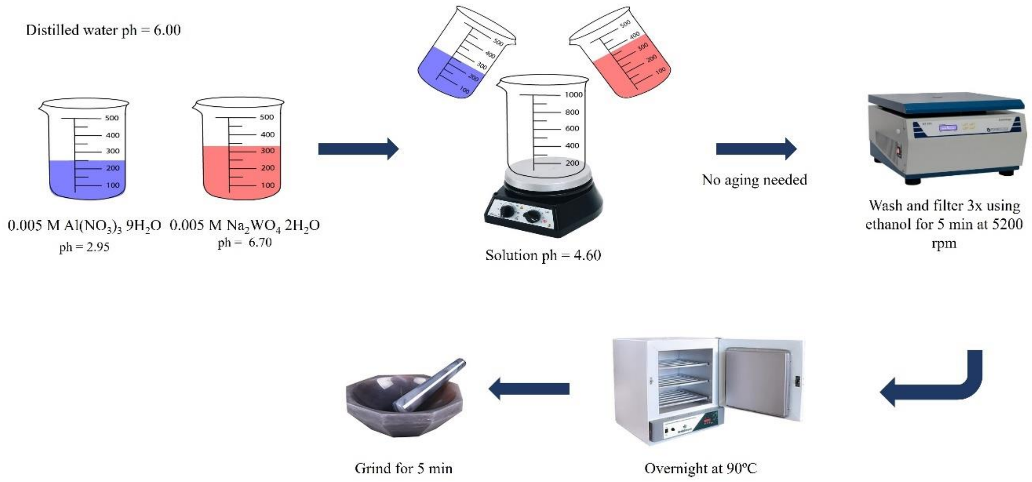

Figure 12: Co-precipitation synthesis of $Al_2W_3O_{12}$.

The aqueous solutions of the reagents were mixed, and white precipitates were formed immediately. The as-formed dispersion was centrifuged at 5000 rpm for 5 min and further washed with ethanol 3 times for 10 min. The obtained white powder was dried in a furnace at 90 °C overnight. Then, the as-prepared amorphous powder was manually ground with a pestle in an agate mortar to break soft agglomerates and calcined in a Clasic elevator furnace coupled with Superkanthal heating elements, at temperatures ranging from 500 to 620 °C, for 20 min. The calcination time was chosen based on previous tests, where it was determined that 20 min was the fastest calcination time to produce orthorhombic $Al_2W_3O_{12}$. The samples were labeled as Axxx for facile comprehension, where xxx stands for the calcination temperature. As the temperature of the calcination increased, the precursor powder gradually changed its color from white to dark gray, at 500 °C, followed by conversion back to white, at 620 °C, as demonstrated in Figure A1 (Appendix).

4.2.2
Characterization

The crystallization temperature and mass losses of the amorphous powder precursor were analyzed by DSC and TG techniques, with a Netzsch STA 449 F3 Jupiter, using approximately 10 mg of powder into an alumina crucible and applying a heating rate of 5 °C min^{-1}, under a static air flow of 50 mL min^{-1}, within the temperature range between room temperature and 900 °C.

The phase composition was verified by XRPD at room temperature. The measurements were carried out using a Rigaku Smart-Lab X-ray diffractometer operating at 3 kW, using Bragg-Bretano geometry, with Cu Kα radiation (1.5406 Å), in the range of 10−90° (2θ), with 0.02° (2θ) step, and a scan speed of 3° min^{-1}. The as-acquired diffraction patterns of the orthorhombic $Al_2W_3O_{12}$ were used, furthermore, to calculate the unit-cell parameters by the Pawley method using Topas software (Bruker), version 5.[59] The morphology and crystallinity were evaluated by Transmission Electron Microscopy (TEM) using a Thermo Fisher Talos F200X G2 operating at 200 kV. A small amount of $Al_2W_3O_{12}$-based powder calcined at 500, 530, and 620 °C was dispersed ultrasonically in ethanol for 20 min and dripped into a copper grid with a lacey 200 mesh carbon film deposition. The TEM images are shown in Figure A3 (Appendix).

DRS absorption spectra were acquired using a PerkinElmer Lambda 650 UV−Vis spectrophotometer, in the range of 250−800 nm and 1 nm step, using α-Al_2O_3 as reference. The collected data were used to evaluate the apparent intrinsic band gap energy of the calcined samples using the Tauc plot evaluated using the Kubelka−Munk function, applied in this study for indirect semiconductors, and to elucidate the light absorption in the visible range. Raman and EPR spectroscopies were used to identify the formation of oxygen vacancies and their concentration, respectively. Raman spectra were obtained with a confocal Witec Alpha 300R equipped with an optical microscope of 200 nm resolution. No special sample preparation was required. A green laser of 532 nm wavelength and 45 mW power was used as the excitation source.

X-band EPR measurements were carried out in a spectrometer, assembled with a JEOL JM-PE-3 resistive magnet using a Magnettech MXH2 microwave source and control unit, with a magnetic field modulation amplitude of 0.92 G at 100 kHz, 20 mW of microwave power, and 60 s scans. The sample's g splitting factor was calibrated using a MgO:Cr3+ standard sample (g = 1.9797) with a known concentration of spins. The oxygen vacancy concentration was determined by fitting the areas of the EPR signals of the investigated samples and the standard MgO:Cr3+ sample. The areas of the signals were compared with the area of the standard sample to determine the spin concentration since the EPR signal is directly proportional to the number of spins presented in a sample. The spin value was divided by the measured mass of each sample and then multiplied by the $Al_2W_3O_{12}$ theoretical density to obtain the spin density and hence the oxygen vacancy concentration.[60]

The surface composition was evaluated via XPS analysis, performed with a Kratos AXIS Supra using a monochromatic Al Kα (1486.7 eV) excitation source and 15 mA of current. The carbon 1s signal (situated at 284.8 eV) was used to calibrate the energy scale of the XPS spectra. The spectra were deconvolved using Casa XPS software.[61]

4.3

Results and Discussion

4.3.1

Crystallization study

DSC, TG, and DTG curves of the amorphous powder heated from room temperature to 900 °C in static air are presented in Figure 13.

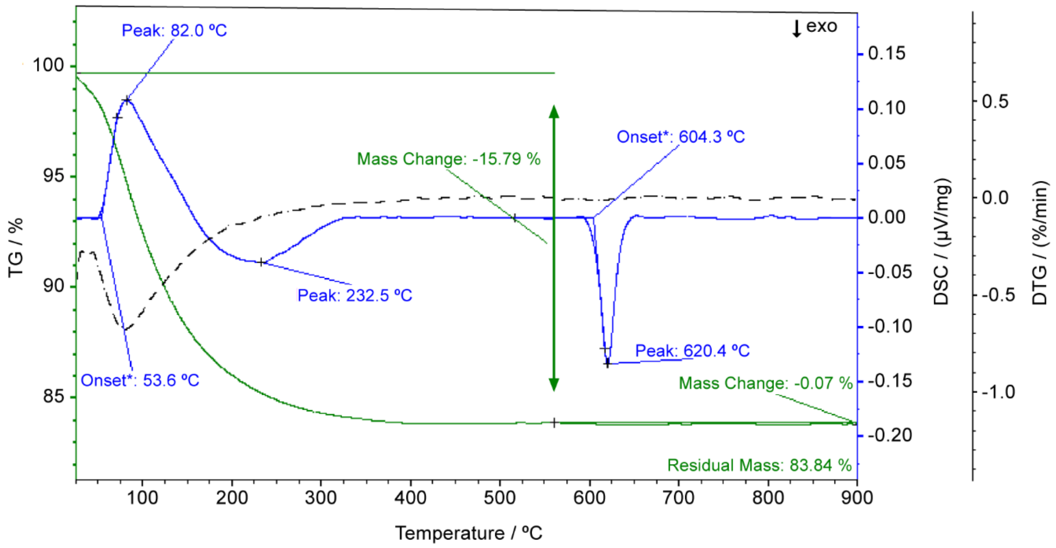

Figure 13: DSC/TG/DTG curves of the $Al_2W_3O_{12}$-based amorphous precursor from room temperature to 900 °C. Exothermic peaks are oriented downwards. The dashed curve stands for DTG.

According to the DSC and TG curves, there are two major events presented by the amorphous powder upon heating: one endothermic and another exothermic. The endothermic event represented by the peak centered at 82 °C, with an onset temperature of 53.6 °C, can be assigned to absorbed water release, while the weight losses above 175 °C can be attributed to the release of hydroxyl groups [49,62–64]. The release of hydroxyl groups is related to the hydroxide-based precursors formed on the co-precipitation of $A_2M_3O_{12}$-based amorphous powders [62]. A total weight loss of 15.8% was recorded until 560 °C. Above 560 °C, the weight loss is negligible (0.07%), suggesting the temperature interval for the crystallization of orthorhombic $Al_2W_3O_{12}$.

In accordance with some previous studies such as the one carried out by Pontón et al. for $Y_2W_3O_{12}$ [62], the coprecipitated amorphous powder in the $A_2M_3O_{12}$ family is an oxyhydroxide(nitrate) compound, which loses weight at temperatures lower than 550 °C (Figure 13). Additionally, the hydroxide-based reagents used in the co-precipitation synthesis of $Al_2W_3O_{12}$-based amorphous powder produce hydroxyl groups which are released above 175 °C.

Recently, Fu et al. reported that a weak endothermic peak, observed in the TG curves of $MgFe_2O_4$ [49], could be associated with oxygen release from the spinel structure, which could cause the formation of oxygen vacancies along the surface of the material.

DSC curve was additionally used to determine the crystallization temperature of orthorhombic $Al_2W_3O_{12}$, which is represented by the exothermic peak centered at 620.4 °C. The crystallization peak has an onset temperature of 604.3 °C; however, as shown in Figure 14 (vide infra), the orthorhombic $Al_2W_3O_{12}$ starts to form at isothermal conditions, at a much lower temperature (510 °C).

The XRPD patterns of amorphous powder and the powders calcined in air in the temperature range between 500 and 620 °C, are shown in Figure 14.

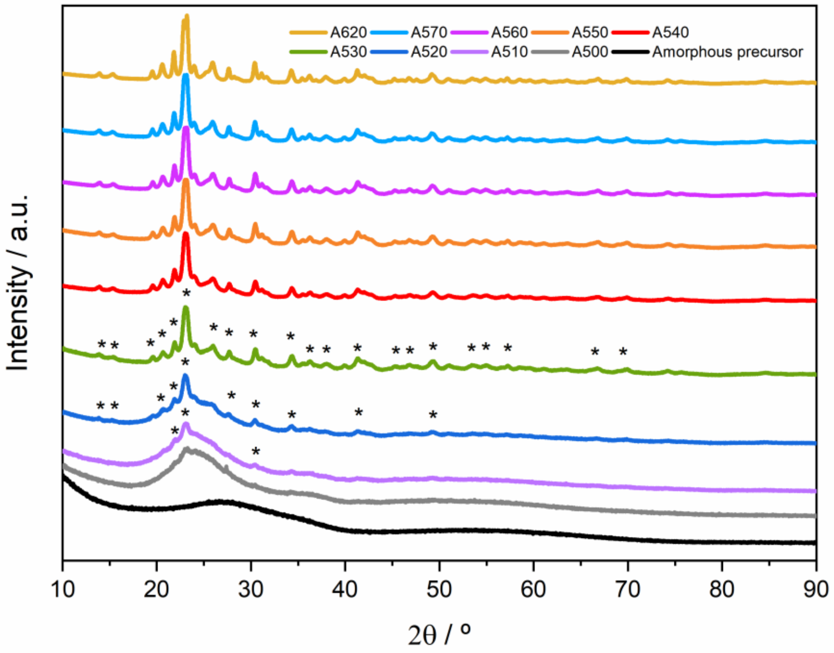

Figure 14: XRPD patterns of the as-prepared $Al_2W_3O_{12}$-based amorphous precursor and the powders calcined in air between 500 and 620 °C. The diffraction peaks belonging to the orthorhombic phase are marked by a star symbol for the samples A510, A520, and A530.

The calcination process in air atmosphere led to a phase transformation from the amorphous state to a crystalline one as shown by XRPD patterns. The amorphous precursor, as well as the calcined sample A500, did not exhibit diffraction peaks, but only an amorphous halo between 18.7 and 30.3° (2θ) indicating its amorphous nature, although the A500 powder changed color to dark gray, in comparison to the white amorphous powder obtained by co-precipitation, which could be an indication of structural and chemical changes, most likely caused by the formation of oxygen vacancies.

In addition, the peak of the amorphous halo was shifted to around 23.7° (2θ) for A500, in comparison to the amorphous precursor, where the amorphous halo is centered near 27.3° (2θ), indicating the start of the internal structure reorganization. The peaks identified in the A510 sample, represented by the star symbol in Figure 14, close to 23.0, 30.4, and 34.2° (2θ) suggest the onset of crystallization. Besides, the samples A520 and A530 exhibit more diffraction peaks belonging to the orthorhombic phase of $Al_2W_3O_{12}$ [65], as well as a prominent amorphous halo, while the color of the powders changed from dark gray to a slightly lighter gray. Thus, at these temperatures, the material was still a mixture of amorphous and disordered orthorhombic structures with a high concentration of extrinsic point defects (determined by EPR, vide infra). The orthorhombic $Al_2W_3O_{12}$ became predominant at 540 °C and was fully crystallized at 620 °C (Pawley refinement data are shown in Figure A2, Appendix).

TEM analysis of the powders calcined at 500, 530, and 620 °C (Figure A3, Appendix) shows the changes across the three main stages, i.e., amorphous at 500 °C, partially crystallized at 530 °C, and fully crystallized at 620 °C. The amorphous sample, A500, exhibited particles with round edges and without a defined format. In addition, crystallographic planes, characteristic of crystalline materials, were not observed. Sample A530 exhibited particles with a mixture of soft round edges and sharp edges, containing regions with well-defined crystallographic planes. Sample A620 has mostly sharp edges, with a particle size higher than 50 nm, showing crystallographic planes typical for a fully crystallized sample, in accordance with XRPD data (Figure 14).

It is known that the formation of point defects can distort the crystal structure [9,45]. Unit-cell volumes of orthorhombic $Al_2W_3O_{12}$ (Table A1, Appendix), as calculated by the Pawley method, resulted in a volumetric expansion of 0.36% for the $Al_2W_3O_{12}$ formed at 540 °C in comparison to the one formed at 620 °C. Another indicator of the formation of extrinsic point defects is the color of the samples (Figure A1).

The XRPD results (Figure 14) evidenced a decrease in the lattice parameters of $Al_2W_3O_{12}$, and an increase in crystallinity, as the calcination temperature increases, due to crystal structure ordering and, probably, oxygen reentering in the lattice, consequently, reducing extrinsic oxygen vacancy content.

Interestingly, crystallization is preceded by the formation of an oxygen-defective amorphous structure at 500 °C, most likely due to partial loss of oxygen during water and hydroxyl group release from the amorphous oxyhydroxide(nitrate) compound, while above 530 °C, the crystal structure started to be predominant and richer in oxygen. In addition, as the calcination temperature increases above 530 °C the structure becomes more ordered and richer in oxygen, with fewer extrinsic oxygen vacancies (Table A2, Appendix) until $Al_2W_3O_{12}$ formed at 620 °C is almost free of extrinsic oxygen vacancies.

4.3.2

Optical properties study

The as-synthesized amorphous powder is white, and after calcination in air at 500 °C, it becomes dark gray, suggesting a high concentration of point defects. As the heat treatment temperature increases, the $Al_2W_3O_{12}$ powders change color from dark gray (A500) to white (A620) suggesting that the extrinsic oxygen vacancy content is decreasing. $A_2M_3O_{12}$-type materials are known wide-band-gap semiconductors that do not absorb light within the visible range [9,66,67], therefore, the color of the powders could be an indicator of the presence of point defects.

This feature was also found in oxygen-deficient $Al_2W_3O_{12}$ [9] heat-treated at 400 °C in H_2 atmosphere, turning the powder dark gray when compared to white extrinsic defect-free powder calcined at 800 °C. Additionally, its unit-cell volume exhibited a 0.2% expansion compared to the extrinsic defect-free phase calcined at 800 °C.

DRS spectra of the calcined $Al_2W_3O_{12}$ powders, especially at lower temperatures (from 500 to 570 °C), Figure 15a, suggest a higher absorption in the visible region, which can be attributed to the introduction of extrinsic point defects formed during the heat treatment in air [9,66].

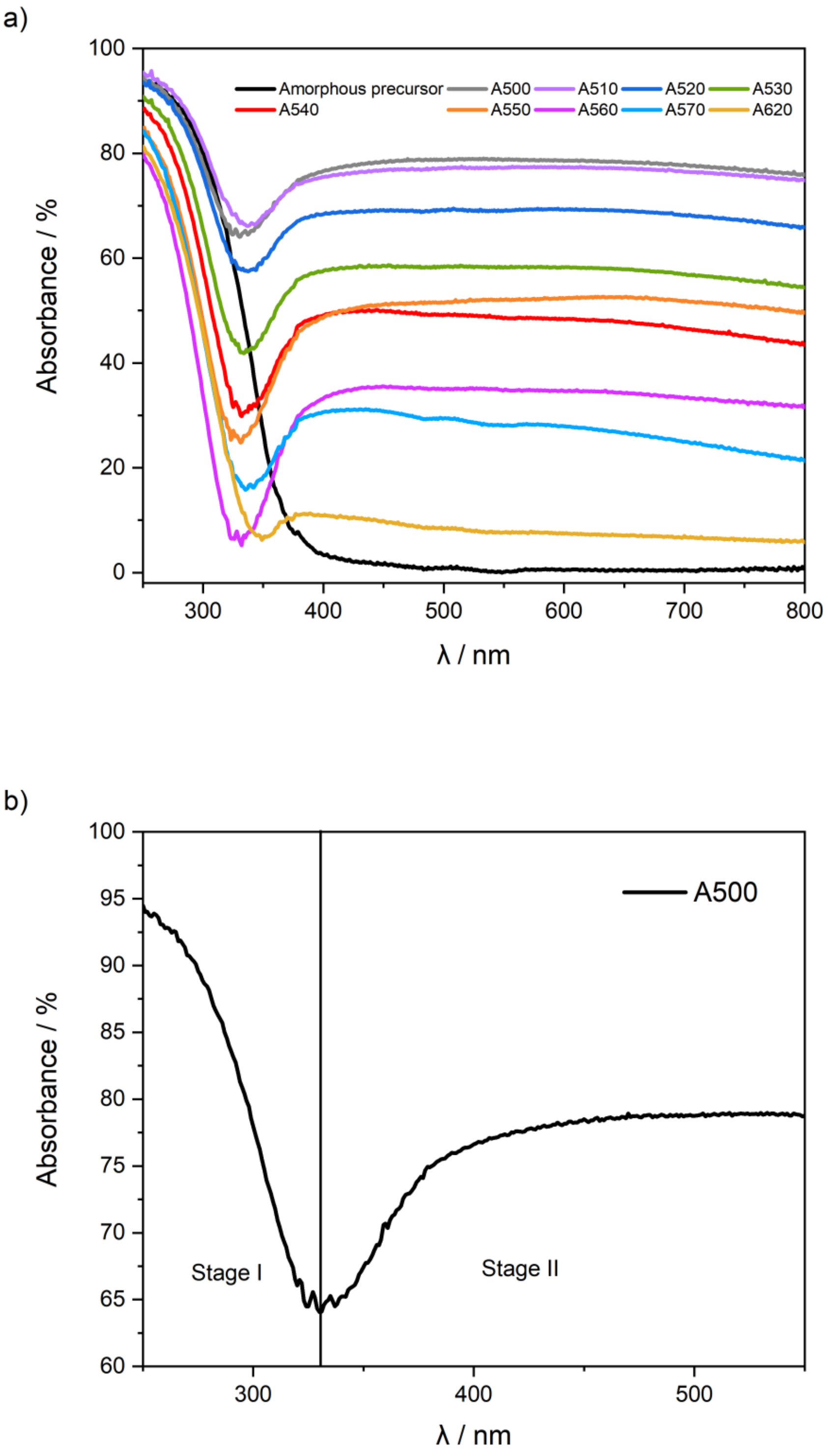

Figure 15: DRS spectra of a) the as-prepared $Al_2W_3O_{12}$-based amorphous precursor and the powders calcined in air between 500 and 620 °C, b) DRS spectrum of the powder calcined at 500 °C illustrating two electronic transitions common for all calcined samples.

The relative intensities of light absorption in the visible range gradually decrease as the calcination temperature increases, reaching at 620 °C a much lower absorption level than the one exhibited by the powder calcined at 500 °C. Therefore, the enhancement of light absorption at lower calcination temperatures can be due to a higher concentration of extrinsic oxygen vacancies (determined by EPR, vide infra) which agrees with the color changes (Figure A1, Appendix) and volumetric expansion (Tables A1 and A5, Appendix) observed in these samples.

All calcined samples displayed two electronic transition stages, as illustrated in Figure 15b. An analysis of the DRS spectra (Figure 15b) showed that the first stage represents the electronic transition between the valence and conduction bands. It is related to the intrinsic behavior of the material as a wide-band-gap semiconductor with an intrinsic band gap energy of around 3.70 eV, as observed in the Kubelka−Munk function plot of the sample calcined at 620 °C (Figure A4, Appendix), close to the intrinsic band gap previously reported for $Y_2Mo_3O_{12}$ [68] of about 3.6 eV. The absorption within the visible range (second stage) represents the electronic transition which can be attributed to the formation of point defects such as oxygen vacancies as demonstrated by EPR (Figure 16).

4.3.3
Oxygen vacancies study and volumetric expansion calculation

EPR was conducted to confirm the presence of oxygen vacancies in the $Al_2W_3O_{12}$ powders.

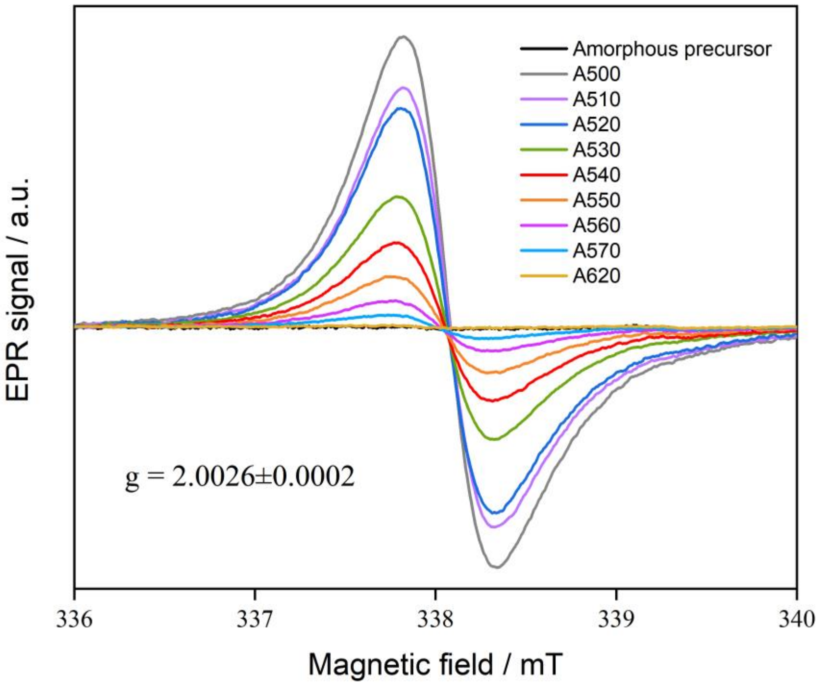

Figure 16: EPR spectra of the as-prepared $Al_2W_3O_{12}$-based amorphous precursor and the powders calcined in air between 500 and 620 °C.

As shown in Figure 16, a significant paramagnetic signal was detected at g = 2.0026, especially for the samples calcined from 500 to 570 °C. The g-factor between 2.001 and 2.004 is commonly attributed to a single electron trapped in oxygen vacancy (SETOV) [49,69]. A particularly high concentration of extrinsic oxygen vacancies was found as the calcination temperature decreased, while sample A500 has the highest concentration of oxygen vacancies (estimated at 6.66×10^{17} cm^{-3}), which can be related to its oxygen-deficient amorphous structure due to structural changes during the reorganization of the lattice and the loss of volatiles, as suggested by XRPD (Figure 14) and DSC/TG (Figure 13), respectively.

In addition, it is worth mentioning that the co-precipitated amorphous powder did not present the signal at $g \sim 2$, indicating that the sample was free of extrinsic oxygen vacancies, while the crystalline A620 sample presented a negligible amount of oxygen vacancies (3.48×10^{15} cm^{-3}), suggesting that the sample is almost free of extrinsic oxygen vacancies. The SETOV concentration decreased about 20 times (Table A2, Appendix) as the heat treatment temperature increased, from 6.66×10^{17} cm^{-3} for A500 to 3.39×10^{16} cm^{-3} for A570, evidencing the decrease in disorder within the orthorhombic crystal structure with the increase of the calcination temperature, also affected by the reentrance of oxygen in the lattice during calcination at higher temperatures, such as 570 °C.

Although sample A620 exhibited a very weak signal associated with SETOV suggesting a negligible amount of oxygen vacancies in the samples, its DRS spectrum (Figure 15a) ratifies that a small amount of extrinsic point defects is still present in the sample due to the presence of a second electronic transition, also observed for the remaining calcined samples.

Figure 17 shows the Raman spectra of the $Al_2W_3O_{12}$ powders with different oxygen vacancy concentrations.

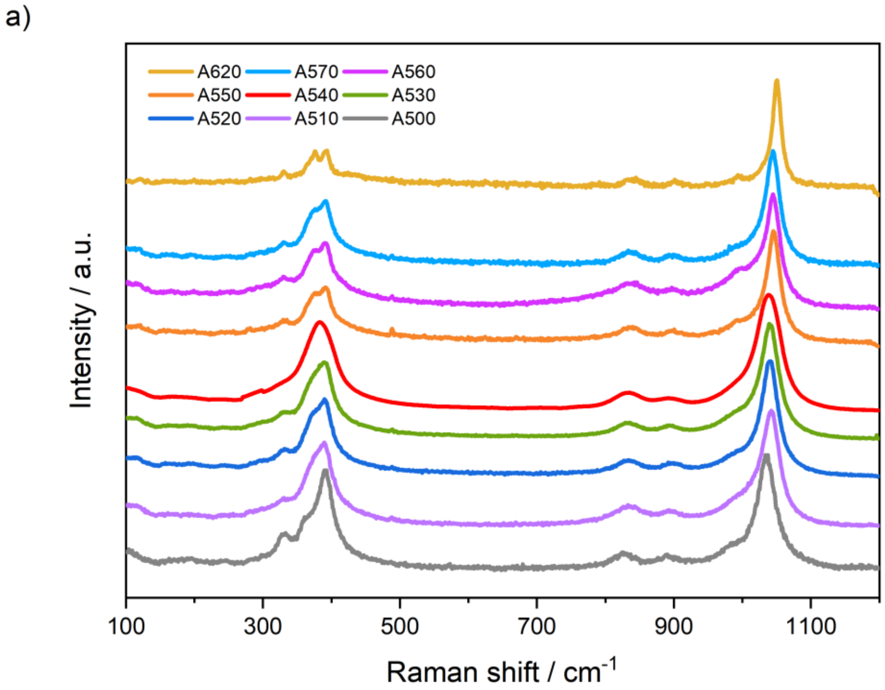

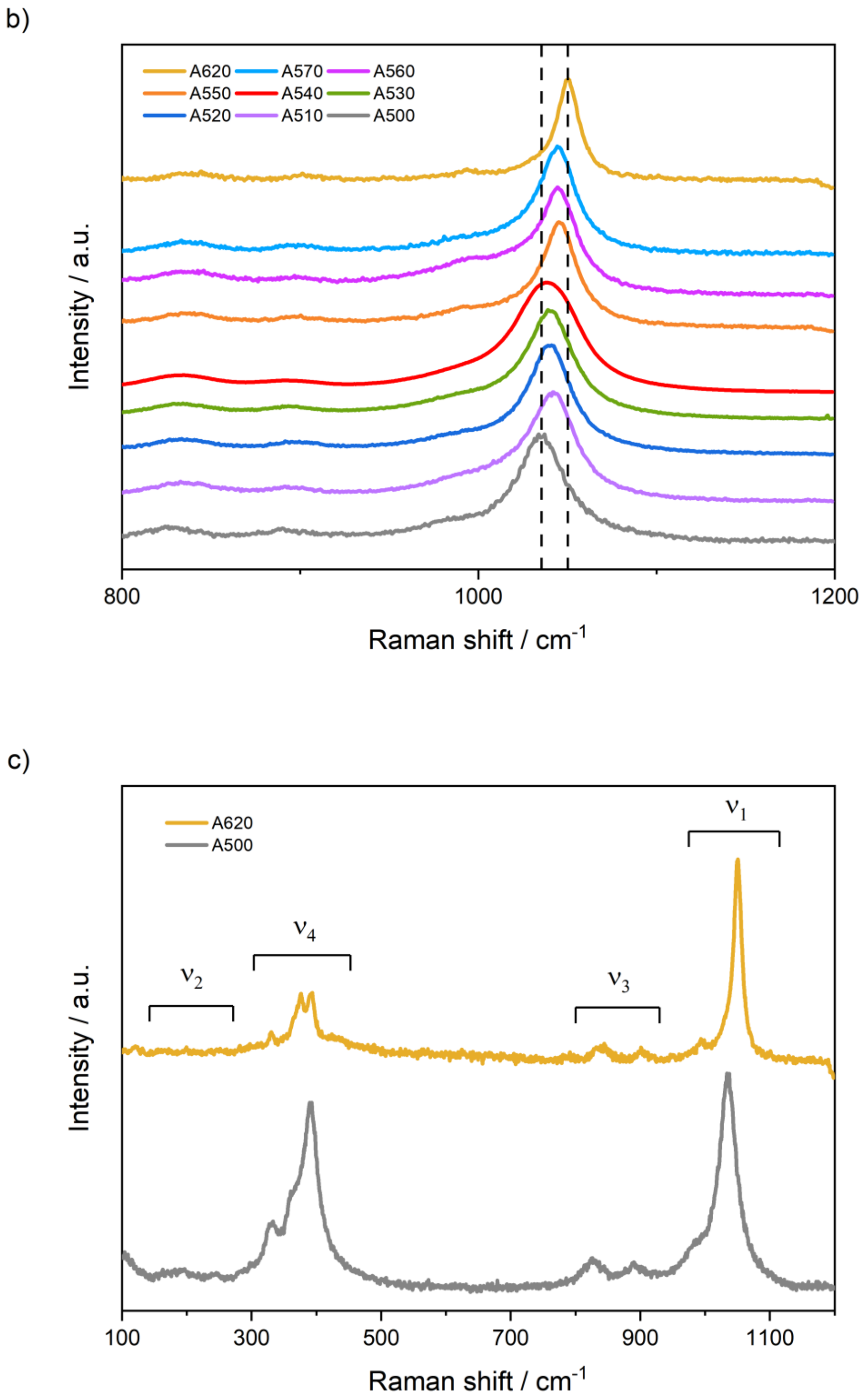

Figure 17: Raman spectra of $Al_2W_3O_{12}$ powders calcined in air between 500 and 620 °C within a) 100−1200 cm^{-1}, b) 800−1200 cm^{-1}, and c) Raman spectra of the powders calcined at 500 and 620 °C. The vertical dashed lines illustrate the red shift of the symmetric stretching vibrations with the decrease in calcination temperature. The vibration modes are marked by the bracket symbol.

Raman spectroscopy was conducted to identify the vibrational changes of the bonds. Several vibrational bands were observed in the 100−1200 cm^{-1} range, divided into four main groups. The range between 950 and 1100 cm^{-1}, presented the most intense band, belonging to W−O symmetric stretching vibrations (ν1), the double peaks in the region of 800−900 cm^{-1} belong to W−O asymmetric stretching vibrations of WO_4 tetrahedra (ν3). The bands around 300−450 cm^{-1} belong to O−W−O bending modes in WO_4 (ν4), while the lower bands situated in the range between 100 and 300 cm^{-1} belong to translational and lattice vibrations of WO_4 tetrahedra (ν2) [70–72].

It was also noticed that the main peak belonging to the O−W−O bending modes, ν4, starts to split into two as the calcination temperatures increase, at around 550 °C, becoming prominent at the highest calcination temperature of 620 °C when the $Al_2W_3O_{12}$ orthorhombic structure is fully formed and almost free of extrinsic point defects (as demonstrated by EPR, vide infra). This feature is commonly reported for highly ordered orthorhombic $Al_2W_3O_{12}$ [70–72], which could represent the strengthening of the O−W−O band due to oxygen enrichment into the crystal structure.

As shown in Figure 17b, as the calcination temperature decreases, a shift of the symmetric stretching band towards lower wavenumber (i.e., red shift) was noticed. The red shift of 15.2 cm^{-1} observed for the symmetric stretching vibration situated close to 1050 cm^{-1}, noted for A500 in comparison to the A620 sample, can be an indication of the presence of extrinsic oxygen vacancies within the A500 amorphous structure since the distortion of the local structure can cause a softening of the W−O bonds [6,45].

On the other hand, as the calcination temperature rises, the structure becomes more ordered, richer in oxygen, and crystalline, and W−O bonds become stronger, which is demonstrated by higher frequencies (wavenumbers) of symmetric stretching vibration. These findings agree with the XRPD, DRS, and EPR results and with the analysis reported by Moreno Diaz et al. for the defective $Al_2W_3O_{12}$ [9]. In addition, the bond distance between the W and O ions was calculated according to the empirical equation (13) proposed by Hardcastle and Wachs [73]

$$\nu = 25823\exp\left(-1.902R\right) \qquad (13)$$

where ν is the wavenumber in cm^{-1}, and R is the metal-oxygen bond length, i.e., interatomic distance given in Å. The sample A620 exhibits a bond distance of 1.6836 Å, while A540 and A500 exhibit bond distances of 1.6895 and 1.6915 Å, respectively. Therefore, the observed red shift of 15.2 cm^{-1} is related to the softening of the bonds due to the introduction of oxygen vacancies.

Accordingly, the red shift is associated with a 1.06% volumetric expansion of WO_4 tetrahedra for $Al_2W_3O_{12}$ in the A540 sample, in comparison to the WO_4 in A620, estimated from the bond distances (see Appendix A5 for the calculation of the volumetric expansion of regular tetrahedra). The volumetric expansion of 0.36% of the unit-cell volumes for A540 and A620 samples, respectively, is lower than the volumetric expansion of WO_4 tetrahedra (1.06%) since the WO_4 tetrahedra are part of the framework of $Al_2W_3O_{12}$ and do not contribute solely to the overall dimensions of the unit-cell.

4.3.4

Charge compensation study

XPS spectra were acquired to determine the valence states of tungsten on the surfaces of the $Al_2W_3O_{12}$ powders.

a)

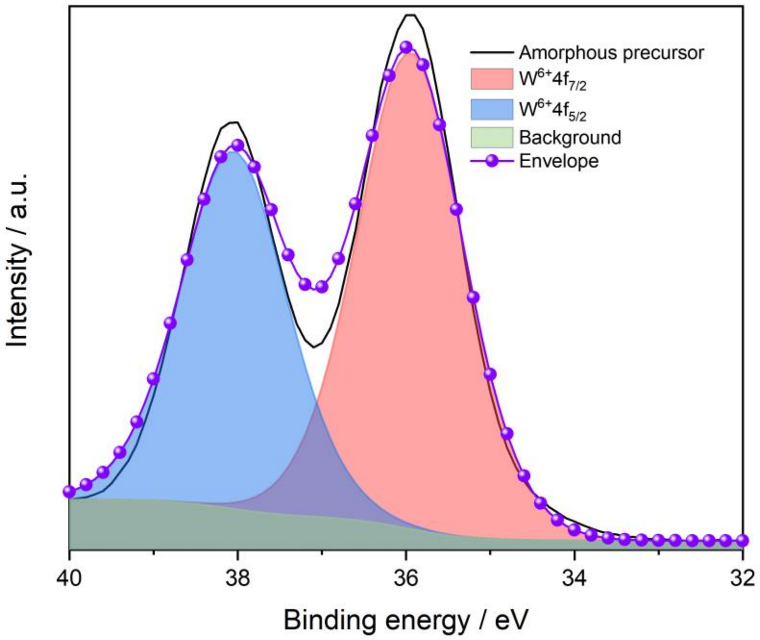
Amorphous precursor
W6+4f7/2
W6+4f5/2
Background
Envelope
Intensity / a.u.
40
38
36
34
32
Binding energy / eV

b)

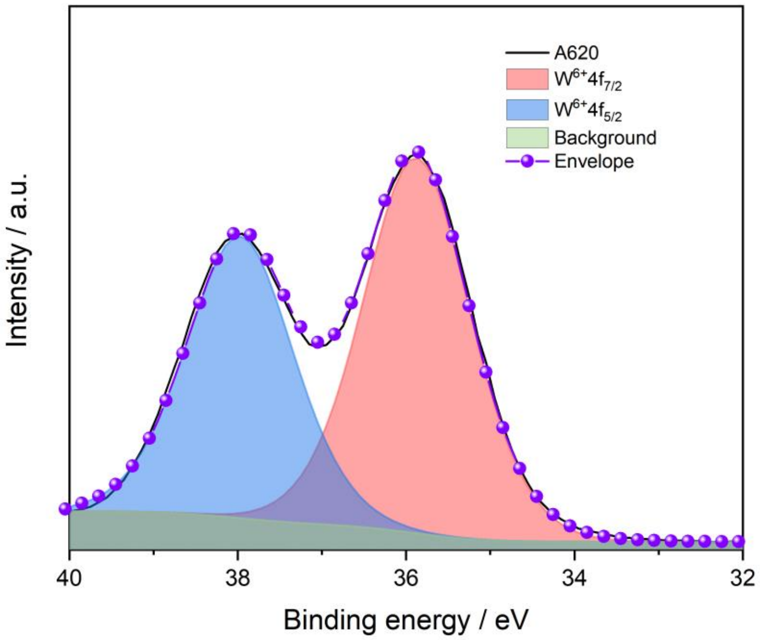
A620
W6+4f7/2
W6+4f5/2
Background
Envelope
Intensity / a.u.
40
38
36
34
32
Binding energy / eV

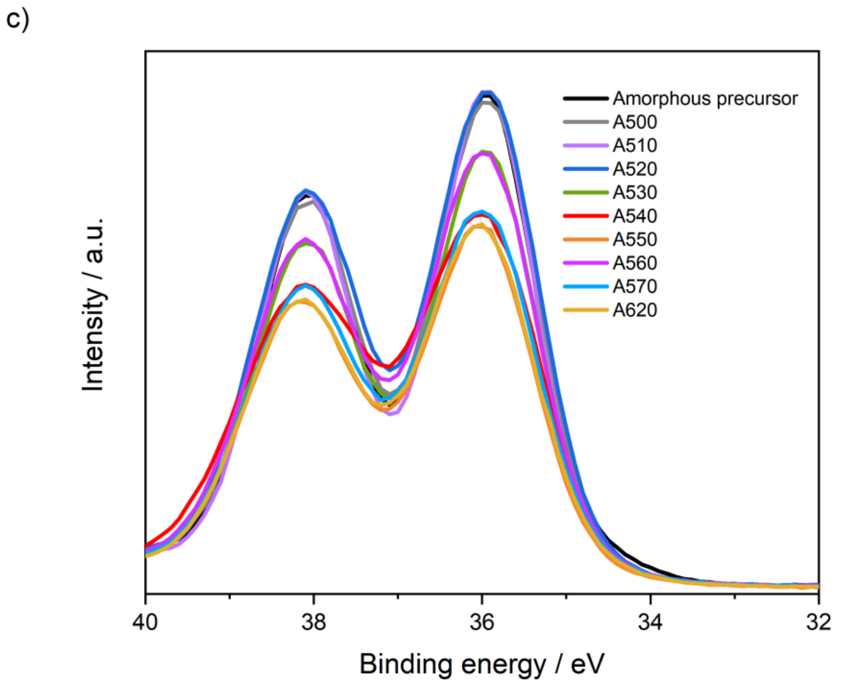

Figure 18: XPS spectra of a) amorphous precursor, b) A620, and c) amorphous precursor and all calcined $Al_2W_3O_{12}$ powders.

As shown in Figure 18, W_{4f} spectra were acquired for the (a) amorphous precursor powder, (b) A620, and (c) all calcined powders. All $Al_2W_3O_{12}$ powders exhibited two peaks centered at around 35.9 and 38.0 eV, which were attributed, respectively, to the $W_{4f7/2}$ and $W_{4f5/2}$ spin−orbit doublets with a separation distance of 2.1 eV [74,75].

In addition, it is known that a material can present two types of charge compensation, ionic and electronic [74–77]. The first type of charge compensation mechanism, known as ionic, causes the formation of W^{5+} or W^{4+} species [74–77], which were not found in the studied powders. XPS spectra indicate that only W^{6+} is present for both amorphous and A620 powders, as well as in all remaining calcined samples (Figure 18c), suggesting that the charge compensation is predominantly electronic.

Differently to the previous findings reported by Moreno Diaz et al., [9] only W^{6+} is found in XPS spectra (Figure 17), suggesting that the charge compensation mechanism is predominantly electronic. As an overall outcome, a 0.36% expansion of the unit-cell volume was observed in this study when oxygen vacancies were introduced for the A540 specimen compared to the A620 sample, suggesting that the oxygen vacancies caused a small distortion of the lattice.

4.4
Conclusions and Future works

This study found that orthorhombic $Al_2W_3O_{12}$ forms through two stages. Firstly, a new amorphous compound, chemically and structurally different from the amorphous state obtained on co-precipitation, is formed at lower temperatures (<530 °C) through reorganization of the original amorphous state and the loss of oxygen, simultaneously with water and hydroxyl groups, causing the formation of extrinsic oxygen vacancies. This is followed, in the second stage, at higher temperatures (>530 °C) by the crystallization of defective crystalline phases with a high concentration of extrinsic oxygen vacancies. Only at temperatures as high as 620 °C an almost extrinsic defect-free orthorhombic $Al_2W_3O_{12}$ is formed due to the enrichment of the crystal lattice by oxygen from the air atmosphere.

EPR corroborated the formation of extrinsic oxygen vacancies, where the sample calcined at the lowest temperature (500 °C) exhibited the highest SETOV content of 6.6×10^{17} cm^{-3}. The correlation between EPR, XRPD, and Raman spectroscopy highlights the distortion of the crystal structure caused by the extrinsic oxygen vacancies. The expansion of the unit cell of the defective orthorhombic $Al_2W_3O_{12}$ is a consequence of the softening of the W−O bonds within the WO_4 tetrahedra. The red shift of 15.2 cm^{-1} observed in Raman spectroscopy suggests a distortion of the lattice, especially at lower temperatures when the crystal structure is still disordered.

XPS results assured that the compensation mechanism at the surface layers occurs predominantly through electronic compensation due to the presence of only W^{6+} species, while EPR corroborates the same compensation mechanism in the bulk.

The findings of this study provide a fundamental understanding of tailoring of $A_2M_3O_{12}$ materials with highly different extrinsic oxygen vacancy concentrations through variations of calcination temperatures (or times) in air atmosphere. As a consequence, this procedure can be used for adjustment of the physical and chemical properties of $A_2M_3O_{12}$ materials, improving their potential.

For future works we plan to evaluate the CTE behavior of the powder as the concentration of oxygen vacancies changes with the calcination temperature, and to evaluate the formation of oxygen vacancies, and its stability, under different gas atmospheres.

5

Rapid densification of low positive thermal expansion $Al_2W_3O_{12}$ ceramics

5.1

Introduction

$Al_2W_3O_{12}$ belonging to the $A_2M_3O_{12}$ family, where A = Al^{3+} to Dy^{3+} and M is usually W^{6+} or Mo^{6+}, which exhibits low-positive, near-zero to negative thermal expansion. Within the $A_2M_3O_{12}$ family, the phenomenon of negative thermal expansion, known as thermomiotic behavior, only occurs in the orthorhombic structure, where, in the open framework, AO_6 octahedra are connected to MO_4 tetrahedra through two-folded oxygen ions[1,78]. The thermomiotic behavior, as well as low-positive to near-zero expansion, can be rationalized through the transversal vibration of the oxygen atoms, which reduces the $A \cdots M$ non-bonding distances and causes a contraction in A-O-M angle [79–81].

Their unusual tunable thermal expansion has spiked the interest in $A_2M_3O_{12}$-type materials since allow different applications, from optical devices, such as sensors [82–87] to electrodes for batteries [88] also being a great candidate for applications that require thermal shock resistance [8,10]. However, the thermal expansion of polycrystalline materials from this family tends to be highly anisotropic, which can cause thermally induced stresses and, consequentially, microcracks [14,18].

$Al_2W_3O_{12}$ is a low-cost and easily synthesized phase presenting low coefficient of thermal expansion. However, a survey of the literature shows the difficulty in obtaining a highly dense, homogeneous, and fine microstructure without microcracks [10,18]. Prisco et al., [10] reported that the tensile strength of $Al_2W_3O_{12}$ decreased to less than 10 MPa when the microstructure was inhomogeneous and coarse-grained, generating microcracks throughout the sintered body. A part of the problem lies in the pre-sintering step, where a deagglomerated powder is necessary to produce dense samples [89,90].

A fine and homogeneous starting powder can lead to better diffusion and, therefore, lower sintering temperatures, allowing a finer microstructure [89,91]. In addition, Sumithra et al. [16] suggested that for $Ln_2W_3O_{12}$ (phase belonging to the $A_2M_3O_{12}$ family) where Ln = La, Nd, Dy, Y, Er, and Yb, large grains combined with a non-homogenous grain shape can lead to extensive microcracking of the sintered ceramic bodies. Therefore, an uneven and larger size starting powder, with low surface area, can cause irreversible microcracks.

Another important factor is the sintering cycle. Conventional techniques (without pressure aid) although able to produce dense ceramics, are time-consuming, while pressure-assisted methods are much faster while it can deal with carbon contamination. The best result for $Al_2W_3O_{12}$ reported for this sintering technique is the three-step sintering (3SS) presented by Prisco et al. [92]. These authors obtained a 96% TD, however, with a relatively low hardness of 500 VHN and medium Young’s modulus of 62 GPa, while the microstructure obtained was coarse-grained. Pressure-assisted methods produce overall better results in terms of microstructure and densification. $Al_2W_3O_{12}$ produced by Spark Plasma Sintering (SPS) obtained a finer microstructure than the one produced by 3SS although it reached the same densification (96% TD), but much higher mechanical properties [92] In addition, Koseva et al., [93] obtained a pellet with 81% TD after 3SS, however, the density of the pellet was increased after hot-pressing (HP), producing a solid with 98.6% TD with higher uniformity in grain size.

A survey of the literature shows that only a few studies compare conventional and pressure-assisted techniques in the $A_2M_3O_{12}$ family. Therefore, the present work aims at a comparative study of Rapid Pressure-Less Sintering (RPLS) and SPS of $Al_2W_3O_{12}$.

5.2
Materials and Methods

5.2.1
Synthesis of $Al_2W_3O_{12}$

The synthesis of $Al_2W_3O_{12}$-based amorphous powder was previously reported in chapter 4.

The as-prepared amorphous powder was manually ground with a pestle in an agate mortar to break soft agglomerates and calcined in a Clasic elevator furnace coupled with Superkanthal heating elements, at 570 ºC for 20 min. The calcination time was chosen after previous tests. Part of the calcined powder was milled in a Planetary Ball Mill Pulverisette 5 Fritsch for 10 min using 5 mm zirconia balls and container.

5.2.2
Characterization

Both $Al_2W_3O_{12}$ powders (milled and non-milled) were uniaxially pressed using a Brio Hranice BSML 21 uniaxial press, using a 5 mm carbon die at 15 MPa for 02 min, producing cylinders of 5 mm height. The cylinders were further cold isostatically pressed using a P/O/Webber KIP 300 E for 05 min at 700 MPa, producing the green bodies used for RPLS sintering.

X-Ray Powder Diffraction (XRPD) was used to evaluate the phase composition of the powders and the sintered pellets. XRPD was performed by a Rigaku X-ray Powder Diffractometer SmatLab 3kW, using Bragg-Bretano setup with Cu-Kα radiation source ($\lambda = 1.54$ Å). Particle size distribution (Dynamic Light Scattering – DLS) of the calcined (non-milled) and milled $Al_2W_3O_{12}$ powders were obtained using an LA950 analyzer. The surface area of both powders was determined using the Brunauer-Emmett-Teller (BET) method, using a QuantaChrome NOVA touch LX2 gas sorption analyzer, after degassing at 120 ºC for 2 h.

The relative densities were obtained after cold pressing and after sintering following the Archimedes method using distilled water (EN 18754). According to experimental data, the theoretical density (TD) of $Al_2W_3O_{12}$ used was 5.082 gcm^{-1}, which is in accordance with previous reports.[65]

The microstructure of the sintered bodies, as well as the calcined powders was verified using a ThermoFisher Verios Scanning Electron Microscope operating at 5 kV. The sintered bodies were previously polished to 1 µm, and thermally etched for 15 min at 700 ºC, then coated using a Leica EM ACE600 Sputter Coater with a 16 nm layer of carbon. The images obtained were used to calculate the grain size distribution using ImageJ, version 1.53.

Vicker's hardness and Young's modulus were measured using the Zwick/Roel Z2.5 hardness testing machine. An indentation of 0.9807 N (HV0.1) was kept for 10 s, and 20 indentations were done per sample. The size of indents was evaluated using a confocal microscope Olympus LEXT OLS 3100.

The coefficient of thermal expansion (CTE) was obtained with a Linseis L70/1700 High-Temperature Dilatometer until 500 ºC, with a heating/cooling rate of 1 ºCmin^{-1}. The CTE was measured in the direction of the applied pressure and perpendicular to it. The CTE was calculated from the cooling part of the shrinkage curve between 450 and 100 ºC according to equation 14 below.

$$CTE = \frac{\varepsilon_{100} - \varepsilon_{450}}{(T_{100} - T_{450}) * 100} \tag{14}$$

where: ε_{100} is the shrinkage after cooling to 100 °C (%), $\varepsilon_{450}$is the shrinkage at 450 °C (%),T_{100} is the temperature of 100 °C (°C), and $T_{450}$is the temperature of 450 °C (°C).

5.2.3
Sintering

The green bodies were first sintered using the dilatometer from room temperature to 1000 ºC, with a heating rate of 10 ºCmin^{-1}, to determine the RPLS sintering temperature. Therefore, the green bodies of both milled and non-milled powder were sintered by RPLS using a Clasic Superkanthal Elevator Furnace with a vertically moving sample holder at 1000 ºC for 10 min and 60 min with a heating rate of 100 ºCmin^{-1}.

SPS experiments were performed using the milled and non-milled powder on a using a Fuji Dr. Sinter 615, with a 10 mm diameter graphite die. The powders were sintered at temperatures 850 ºC and 1000 ºC for 2 min, with a 50 Mpa applied pressure. The heating and cooling rates (100 $^{\circ}\mathrm{Cmin}^{-1}$) were controlled using a pyrometer. The sintering temperature of the SPS was based on the dilatometry performed for the RPLS samples, and further tests lowering the sintering temperature.

The samples were labeled according to the sintering methods and type of powder used (R or S – n or m – temperature/time). For example, S-n-850 corresponds to the SPS sample sintered at 850 ºC using the non-milled powder. However, since all the RPLS samples were sintered at 1000 ºC its notation uses the sintering time instead of temperature, therefore, *e.g.*, the sample R-m-10 corresponds to the RPLS sample sintered at 1000 ºC for 10 min, using milled powder.

5.3
Results and Discussion

5.3.1
$Al_2W_3O_{12}$ powders and green bodies

There are many ways of producing submicronic to nanometric $A_2M_3O_{12}$-type powders, such as coprecipitation, sol-gel, solid-state reaction, and hydrothermal method[19–24]. Truitt et al. [19] produced a submicronic $AlScMo_3O_{12}$ *via* non-hydrolytic sol-gel. Although this method allows for the operation in lower temperatures, it is highly cost-effective and time-consuming. Meanwhile, Nikolov et al., [20] prepared submicronic to nanometric $Al_2W_3O_{12}$ powders *via* solid-state reaction, sol-gel, and coprecipitation synthesis whereas the latter resulted in a nanometric powder ranging from 10 to 40 nm at its best. The $Al_2W_3O_{12}$ powder made by solid-state reaction was a non-homogeneous with the particles ranging from 20 to 120 nm, at its best setting.

Therefore, due to its low-cost and facile synthesis, $Al_2W_3O_{12}$ was produced in this study *via* co-precipitation synthesis. Different authors produced $Al_2W_3O_{12}$

via the same route, such as Prisco et al[10,92] and Nikolov et al. [20]. However, in the present study different precursors and different molarities were used, resulting in a finer amorphous powder of superficial surface area as high as 66.3 m^2g^{-1}, the highest one reported yet, to the best of the author's knowledge. Nikolov et al[20] used the same precursors as in our study, however, with a higher molarity of 0.1 M, and, additionally, the solution was aged for 10 h, which can lead to particle growth and impact negatively sintering [89,90] In this study, a much lower molarity (0.005 M) was used without aging to prevent unnecessary particle growth.

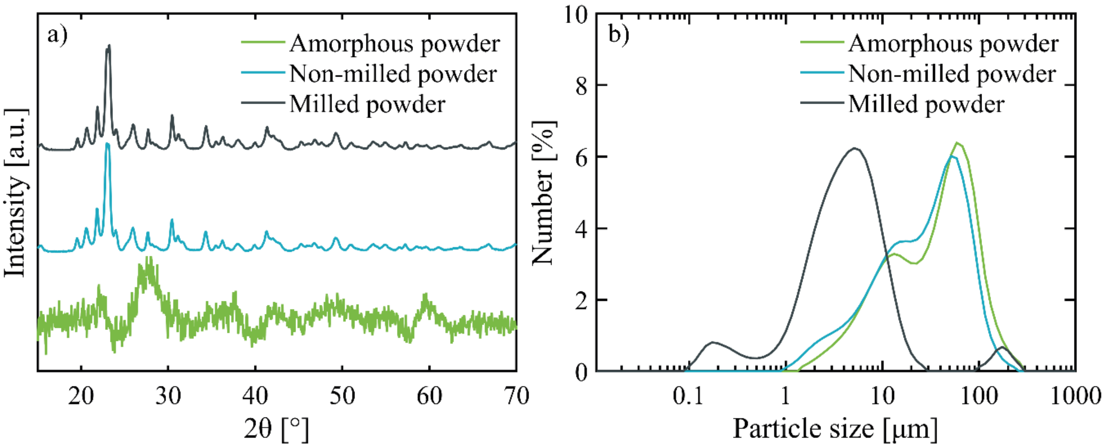

Figure 19: a) XRPD patterns of the amorphous as-synthesized $Al_2W_3O_{12}$ powder and calcined milled and non-milled $Al_2W_3O_{12}$ powders, and b) particle size distribution of amorphous as-synthesized $Al_2W_3O_{12}$ powder and calcined milled and non-milled $Al_2W_3O_{12}$ powders.

XRPD patterns shown in Figure 19a show that the calcination process leads to a phase transformation from amorphous (green curve) to crystalline (blue and grey curves). Additionally, the XRPD patterns confirm that the $Al_2W_3O_{12}$ powders are monophasic and orthorhombic (*Pbcn* space group) [65].

DLS measurements of amorphous and non-milled powders (Figure 19b) suggest a trimodal agglomerate distribution, in which the agglomerates range from 3 µm (first peak), 13 µm (second peak), and 60 µm (third peak), with an average size of d_{50} = 35.8 µm. However, a primary particle size of 18 nm was calculated from BET method, considering spherical particles. SEM micrographs, Figure 20a, show that the primary particles range from 50 nm to 100 nm for all samples. In addition, it can be observed that the powder was heavily agglomerated (See inset in Figure 20a), as suggested by DLS.

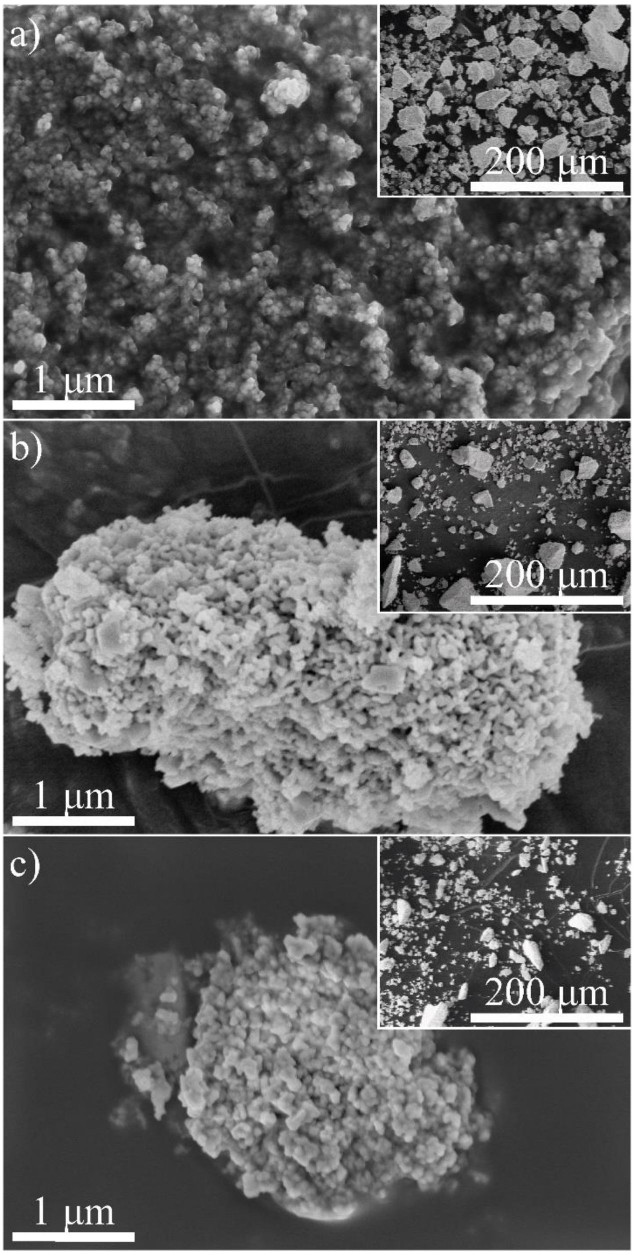

Figure 20: SEM of a) amorphous as-synthesized $Al_2W_3O_{12}$ powder, b) calcined non-milled $Al_2W_3O_{12}$ powder, and c) calcined milled $Al_2W_3O_{12}$ powder.

The calcination process was performed at a lower temperature of 570 ºC, when compared to previous studies, like the one reported by Marzano et al. [24] which used 650 ºC or the one published by Prisco et al.[10] with the calcination temperature of 750 ºC. The calcination at lower temperature was carried out to avoid coarsening of the primary crystallites. This process resulted in a specific surface area of 26.4 m^2g^{-1}, being as high as the previously reported by Marzano et al[24] for $Al_2W_3O_{12}$ produced by non-hydrolytic sol-gel method.

Milling of the calcined powder was performed to increase the specific surface area, since it was noted in the SEM (Figure 20a and b) that both the amorphous and the calcined powders have large agglomerates. Therefore, the calcined powder was ball milled for 10 min to break the soft agglomerates and to avoid contamination from the zirconia balls. This process resulted in a specific surface area of 31.4 m^2g^{-1}, the highest reported so far for this compound [24] According to DLS (Figure 19b), the milling process lowered the agglomeration distribution, where the medium particle size d_{50} is 3.9 μm. Larger agglomerates of approximately 200 μm were observed in the milled powder however, this can be due to artifacts during the measurements [94,95] However, the trimodal distribution of the agglomerates could have prevented further densification of the pellets.

According to SEM micrographs in Figure 20c, the primary particle seems to remain the same size (50 to 100 nm) even after milling. However, it can be seen in the inset of Figure 20c that most agglomerates are indeed broken up after milling. Reduction of the agglomerates size can help decrease shape-related defects during sintering and during green body formation [90]. However, too much milling can introduce defects which are inherent to the milling process and can deform the particles preventing them to form necks and further sinter [96]

The green bodies made with milled powder reached a moderate density of 66.4 % TD, while the green body prepared with the non-milled powders obtained a 64.4 % density, which agrees to those reported in the literature for the same material [10,92,97] The slight improvement in the densification of the green bodies is a result of the milling process.

5.3.2
Dilatometry

The green bodies produced with milled and non-milled powders were submitted to dilatometry to determine the sintering temperature to be used in the sintering experiments. Figure 21a shows the dilatometry curves of the green bodies for RPLS while Figure 21b shows the dilatometric curve obtained along SPS experiments.

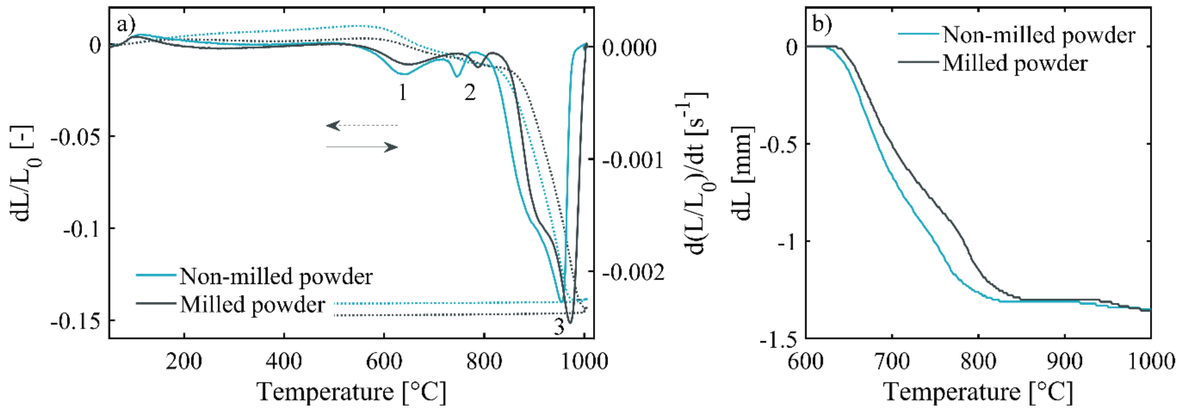

Figure 21: Dilatometric curves from a) high-temperature dilatometry, where shrinkage curves are represented by the dotted lines and their first derivatives are represented by the solid lines, and b) SPS shrinkage curves.

It can be noted that the shrinkage curves of both sintering methods display similar behavior for the pellets formed from milled powder, which shrink at slightly higher temperatures than the non-milled powder (~ 20 ºC). This difference can be caused by the different agglomerate sizes in the non-milled powder, providing a different pore distribution. It is known that an optimized synthesis of ceramic powders results in a finer starting powder with high specific surface area, which allows a lower sintering temperature for both pressure-less and pressure-assisted methods [10,92].

5.3.3

Densification of $Al_2W_3O_{12}$ and phase composition

Two different sintering methods were used in this study, a pressure-less and a pressure-assisted: RPLS and SPS. Some previous studies also reported sintered $Al_2W_3O_{12}$ without pressure aid, such as the one reported by Prisco et al. [10]. The $Al_2W_3O_{12}$ powder produced by Prisco et al. [10] was mixed with binders and sintered at a conventional furnace at 1000 ºC for 10 h. This process resulted in 91 % TD. A more recent study done by the same authors used 3SS to sinter $Al_2W_3O_{12}$, also with the addition of binders, at 900 ºC for 6 h, 1075 ºC for 1 h, and 950 ºC for 6 h, totalizing 13 h, resulting in a higher density of 96 % [92]. In this study, $Al_2W_3O_{12}$ was sintered at 1000 ºC during a considerably lower time (10 and 60 min), reaching densities (95.5 % and 96.0 %) comparable to the ones published so far for pressure-less method. The relative densities obtained for both sintering methods applied in the present study are listed in Table 1.

The high density obtained in this study for the RPLS samples may be attributed to higher heating rates. This feature leads to a temperature homogeneity, preventing the formation of regions with lower temperatures at which a non-densifying surface diffusion path occurs predominantly. In addition, a higher heating rate allows for grain boundary and lattice (volume) diffusions from the grain boundaries toward the necks, accelerating the densification process [98] García et al., [99] suggested that a high heating rate can form an outer layer that is denser than the rest of the sample. This denser outer layer acts as a densification front with higher thermal conductivity increasing heat flux to the sample's interior. As a result, this feature provides more thermal energy for diffusion.

Table 1: Sintering conditions and its respective relative density, Vickers hardness, and Young's modulus.

Sintering regime	Sintering temp. [°C]	Dwell [min]	Powder condition	Label	ρ [% TD]	HV0.1 [GPa]	E [GPa]
RPLS	1000	10	Milled	R-m-10	95.6 ± 0.3	3.8 ± 0.4	46.8 ± 4.5
			Non-milled	R-n-10	95.5 ± 0.3	3.9 ± 0.5	45.4 ± 1.8
		60	Milled	R-m-60	96.0 ± 0.2	3.9 ± 0.6	42.8 ± 3.5
			Non-milled	R-n-60	95.7 ± 0.3	3.9 ± 0.4	45.9 ± 3.4
SPS	850	2	Milled	S-m-850	97.8 ± 0.1	6.9 ± 0.5	64.0 ± 3.3
			Non-milled	S-n-850	97.7 ± 0.1	6.4 ± 0.3	62.3 ± 2.2
	1000	2	Milled	S-m-1000	97.5 ± 0.3	4.0 ± 0.6	51.7 ± 2.7
			Non-milled	S-n-1000	97.1 ± 0.2	3.8 ± 0.6	44.7 ± 2.2

SPS resulted in denser samples, reaching densities as high as 97.8 % when sintering at 850 ºC for 2 min. Interestingly, this study slightly surpasses the densification reported by Prisco et al. [92] where $Al_2W_3O_{12}$ was sintered *via* SPS under the same conditions (1000 ºC for 02 min), reaching a density of 96 % TD. However, the increase in SPS temperature, from 850 ºC to 1000 ºC did not increase the densification, showing a slight decrease in densification from 97.7 % TD to 97.1

% TD for non-milled powder, and from 97.8 % TD to 97.5 % TD for the milled powder. Although the densification was not significantly impacted by the increase in temperature, the microstructure was severely affected (*vide infra*, 5.3.4).

XRPD patterns of the sintered $Al_2W_3O_{12}$ pellets were acquired to confirm their phase composition after sintering *via* RPLS and SPS techniques (Figure 22).

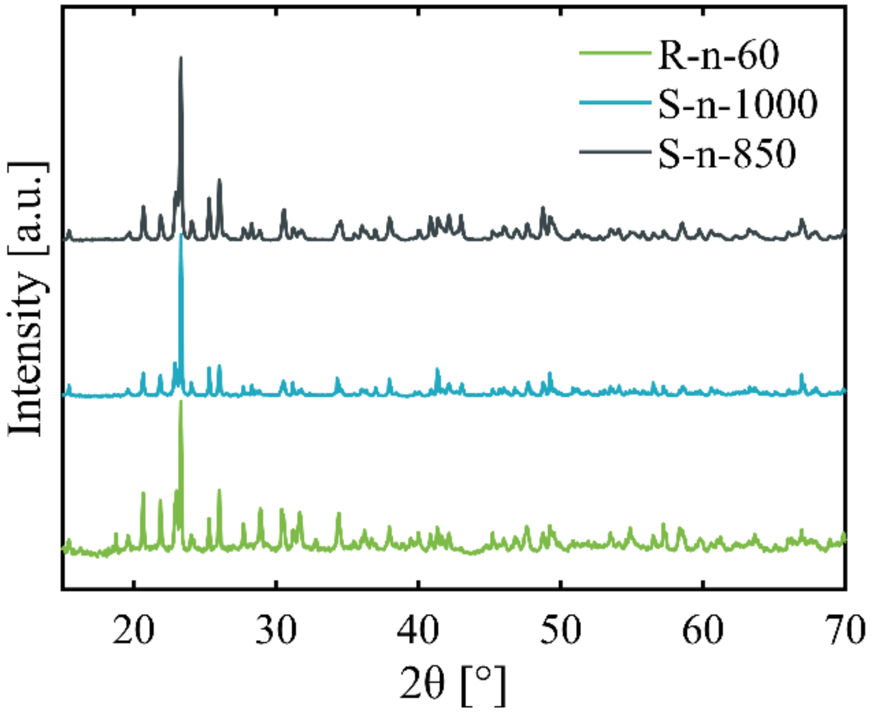

Figure 22: XRPD patterns of the sintered $Al_2W_3O_{12}$ samples.

It can be concluded from the XRPD patterns that the samples remain monophasic with $Al_2W_3O_{12}$ in orthorhombic crystal system.

5.3.4
Microstructure and grain area distribution

SEM micrographs, Figure 23, were used to evaluate the microstructure of the sintered samples. RPLS samples from both milled and non-milled powders displayed the same microstructural behavior. It consisted of coarse and elongated grains in the range between 50 and 150 µm, with intragranular and intergranular porosity. In addition, it was also observed microcracks in all RPLS samples, indicated by the white arrows (Figure 23a).

A similar feature was observed for SPS samples sintered at 1000 ºC (Figure 23b), where coarse and elongated grains were also found, however, they were accompanied by smaller grains (see, black arrows in Figure 23b). Microcracks were also found in SPS samples, marked by the white arrows. Intragranular porosity could be originated from primary pores trapped during grain growth.

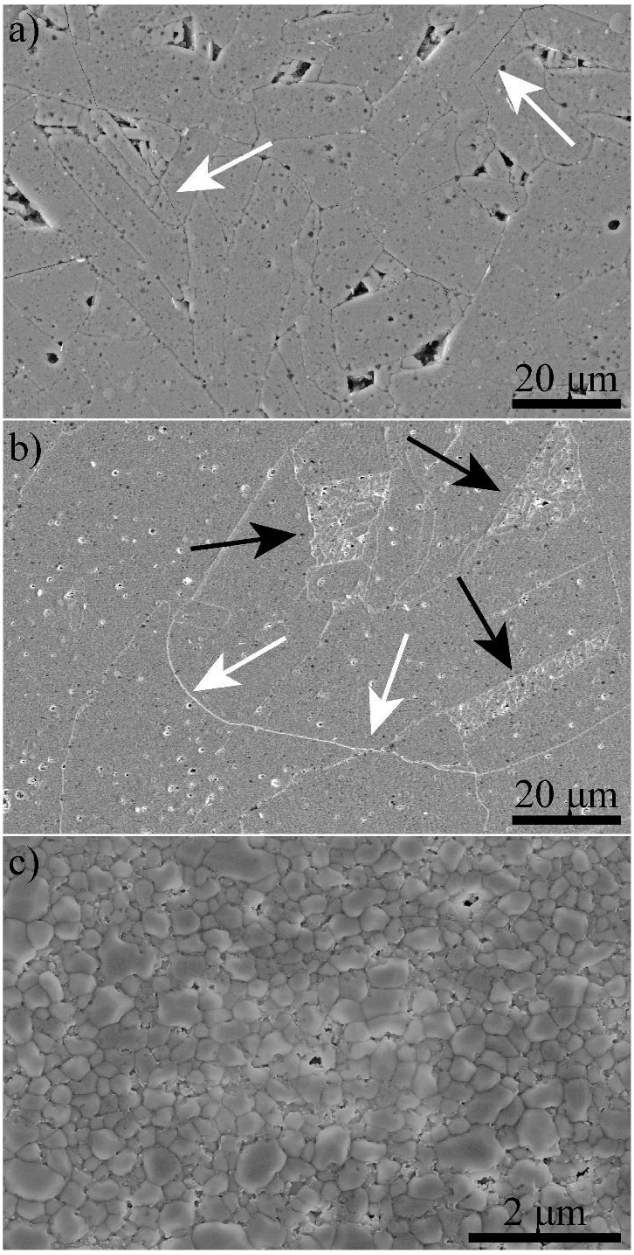

Figure 23: SEM micrographs of $Al_2W_3O_{12}$ sintered by a) RPLS sample R-m-10, b) SPS pellet SPS-m-1000, and c) SPS pellet SPS-m-850.

Some previous reports already showed abnormal grain growth and elongated grains in sintered $Al_2W_3O_{12}$ by pressure-less sintering methods [93,100] Moreover, Koseva et al., [93] observed that nanometric starting powders tend to grow in the preferred crystallographic direction.

SPS pellets sintered at 850 ºC exhibited a very different microstructure from the remaining samples. A fine microstructure of submicronic grains around 400 nm in size, resulted in better densification (97.7 and 97.8 % TD). No microcracking was observed at this sintering temperature for both milled and non-milled starting powders.

Intragranular and transgranular microcracks occurred in all RPLS and SPS samples sintered at 1000 ºC due to CTE anisotropy was stimulated by the formation of coarse and elongated grains. Therefore, it can be assumed that the finer microstructure produced by the lower SPS temperature (850 ºC) prevented microcracking, as well.

The SEM micrographs (Figure 23) were used to calculate the grain area distribution, as shown in Figure 24. RPLS samples present a wide range of grain sizes, ranging from less than 1 μm^2 to hundreds of μm^2. In addition, it can be seen that a shorter sintering time (10 min) was able to form a slightly finer microstructure with slightly smaller grains. It is important to note that in all RPLS samples, the samples produced with milled powder resulted in slightly finer grains, which can be observed by the black curves that are shifted to the left (smaller values).

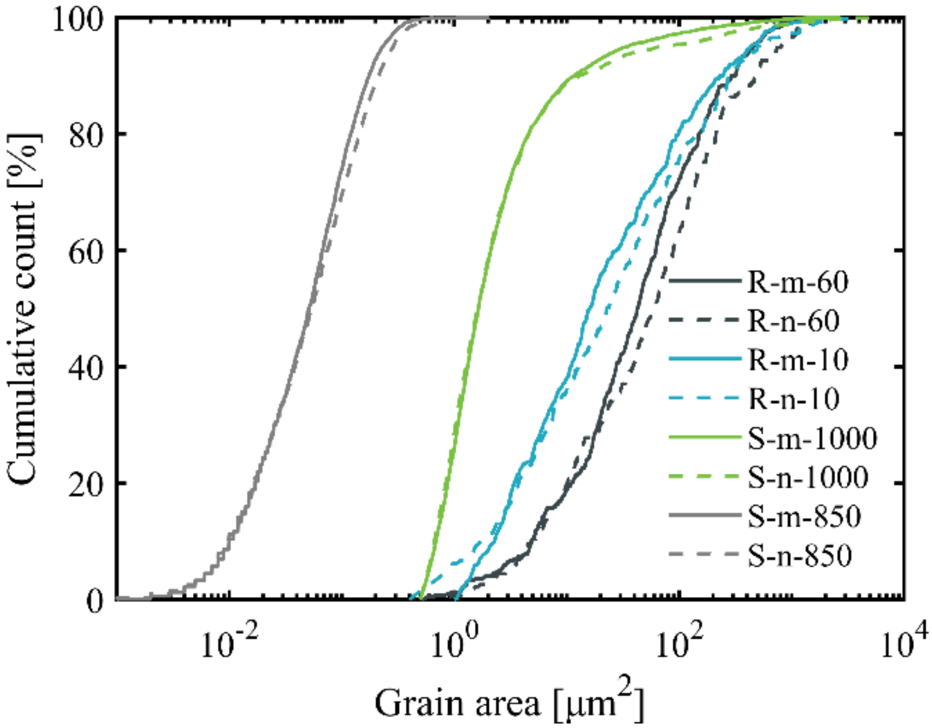

Figure 24: Grain area distribution of the cross-section grain areas of the sintered bodies of $Al_2W_3O_{12}$.

It was observed that SPS sample sintered at 1000 ºC exhibited a cluster microstructure, where larger elongated grains of around 50 – 150 µm surround smaller grains of 1 to 10 µm. SPS sample sintered at 850 ºC produced a finer microstructure with remarkably smaller grains and a narrow grain area distribution between 10^{-2} µm^2 and 1 µm^2.

5.3.5
Coefficient of Thermal Expansion - CTE

The CTE contained in Table 2 was calculated for all RPLS and SPS samples by dilatometry. The measurements were taken in the direction of the applied pressure during sintering (z-axis) for SPS samples and along the pressing direction for RPLS samples, and also perpendicular to it (x and y axes). RPLS samples sintered at 1000 ºC for 60 min presented CTEs between 1.2×10^{-6} K^{-1} for the sample using non-milled powder, and 1.9×10^{-6} K^{-1} for the milled powder, and did not show any significant difference between x, y, and z directions. The calculated CTE values are in accordance with the CTE values reported for polycrystalline $Al_2W_3O_{12}$ ($1.7 - 2.0 \times 10^{-6}$ K^{-1}),[10,92] and also agree with the average value from all crystallographic axes measured from a $Al_2W_3O_{12}$ single crystal (1.5×10^{-6} K^{-1}) [101].

Table 2: CTE measurements in the direction of the applied pressure (z-axis), and along the direction perpendicular to the applied pressure (x and y axes).

Sample	CTE [$\times 10^{-6}$ K^{-1}]
R-m-60-*z*	1.6
R-m-60-*xy*	1.2
R-n-60-*z*	1.7
R-n-60-*xy*	1.9
S-m-850-*z*	4.2
S-m-850-*xy*	2.2
S-m-1000-*z*	6.2
S-m-1000-*xy*	1.4

On the other hand, SPS samples S-m-850 and S-m-1000 exhibited a significant difference in CTE between the axes. This CTE is close to the one reported for a single crystal along the a-axis in the *Pbcn* space group (8.3×10^{-6} K^{-1}) [101] and the CTE values between 5.98×10^{-6} K^{-1} [65] and 6.58×10^{-6} K^{-1} reported for *a*-axis in $Al_2W_3O_{12}$ polycrystalline samples[9] Therefore, it could be suggested that the applied pressure during SPS caused texturization of particles along *a* crystallographic direction, which is in accordance with the pseudo two-dimensional crystal structure of $A_2M_3O_{12}$ phases where b-c layers are connected between themselves along a-direction through few primary bonds [1].

The S-m-1000 sample presented CTE of 1.4×10^{-6} K^{-1} in the direction perpendicular to the applied pressure. According to Imanaka et al., [101] a lower CTE is in accordance with lower CTE in the b and c axes of a single crystal. The SPS-m-850 sample with finer microstructure did not exhibit any apparent abnormal preferentially grain growth, however due to the applied pressure during sintering, the CTE measured in this direction (z-axis) is higher (4.2×10^{-6} K^{-1}) than the CTE measured in the direction perpendicular to the applied pressure (2.2×10^{-6} K^{-1}).

5.3.6

Mechanical properties

The Vickers hardness (HV0.1) and Young’s modulus are summarized in Table 1 (see section 5.3.3). RPLS samples exhibited similar Vickers hardness; 3.8 GPa for the sample R-m-10 and 3.9 GPa for the remaining samples. The RPLS Young’s modulus ranged from 42.8 to 46.8 GPa (milled powders). The sample sintered for 10 min using milled powder displayed a slightly higher Young’s modulus of 46.8 GPa, and the sample sintered under the same conditions using non-milled powder showed a Young’s modulus of 45.4 GPa, Interestingly, the samples sintered for 60 min exhibited an inverse behavior, where the sample sintered using non-milled powder presented a slightly higher Young’s modulus (45.9 GPa) than the one using milled powder (42.8 GPa).

SPS samples sintered at 1000 ºC also had similar Vickers hardness, such as 4.0 GPa for S-m-1000, and 3.8 GPa for S-n-1000. However, Young’s modulus was higher in the S-m-1000 sample (51.7 GPa) than in the sample S-n-1000 (44.7 GPa). Although SPS samples sintered at 850 ºC exhibited little difference in densification when the milled powder was used instead of the non-milled one, a slightly higher Vickers hardness was achieved when milled powder was used; 6.9 GPa for the sample S-m-850, and 6.4 GPa for the sample S-n-850. The Young’s modulus displayed the same behavior where the milled powder presented a slightly higher value of 64 GPa when compared to the non-milled powder (62.3 GPa). However,when compared to the RPLS samples it showed a considerable increase. Although the densities of the samples prepared by RPLS and SPS at their best respectively settings were close to each other (96 and 98 % TD, respectively), the mechanical performance of SPS samples surpassed RPLS samples almost twice, likely due to the finer microstructure of the samples obtained at 850 ºC, in line with the Hall-Petch effect reported for nanoceramics [102]. Therefore, it seems that lowering the sintering temperature in SPS experiments improved both microstructure and mechanical properties.

5.4
Conclusions and Future works

Highly dense, monophasic, and polycrystalline $Al_2W_3O_{12}$ were produced by both RPLS and SPS techniques, where SPS exhibited overall better results. A partially optimization of the synthesis of the starting powder significantly affected primary $Al_2W_3O_{12}$ particles, increasing their specific surface area, allowing better sinterability, thus allowing a lower calcination temperature, which improved mechanical properties. Ball milling of the starting powders improved slightly packing density of the particles, and consequently green body density, although not much improvement was observed in the final densification occurred during sintering. SPS samples exhibited the highest density for $Al_2W_3O_{12}$ reported so far.

RPLS samples reached a 96 % TD in a considerably short time (10 min) and at a similar temperature (1000 ºC) with those reported previously for the same material. However, all RPLS samples displayed coarse microstructure with elongate grains, due to abnormal grain growth, and also presented microcracking. This feature could be a result of an inhomogeneous starting powder as observed by DLS and SEM. The Vickers hardness and Young’s modulus of the samples using milled powder were, respectively, 4 and 47 GPa.

SPS produced microcrack-free and fine microstructure when sintered at 850 ºC. In this setting, the SPS sample using milled powder showed a density as high as 98 % TD, which resulted in improved mechanical response. The Vickers hardness and Young’s modulus of the sample using milled powder were, respectively, 7 and 64 GPa, almost two times higher than those obtained with RPLS.

The future works regarding this chapter consist of the optimization of the starting powder, to obtain a finer and less agglomerated powder and further SPS studies in order to obtain a fully dense $Al_2W_3O_{12}$ ceramics. In addition, Hot Isostatic Pressing or High Pressure High Temperature methods should be studied to improve the densification of the pellets.

6
Appendix

6.1
Supplementary information of chapter 4

A1

$Al_2W_3O_{12}$ powders from amorphous to calcined at 620 ºC and their respective color changes from white for the as-synthesized amorphous powder, to dark gray for the powder calcined at 500 ºC, and again to white for the powder calcined at 620 ºC. The powders are contained in an HDPE sample holder.

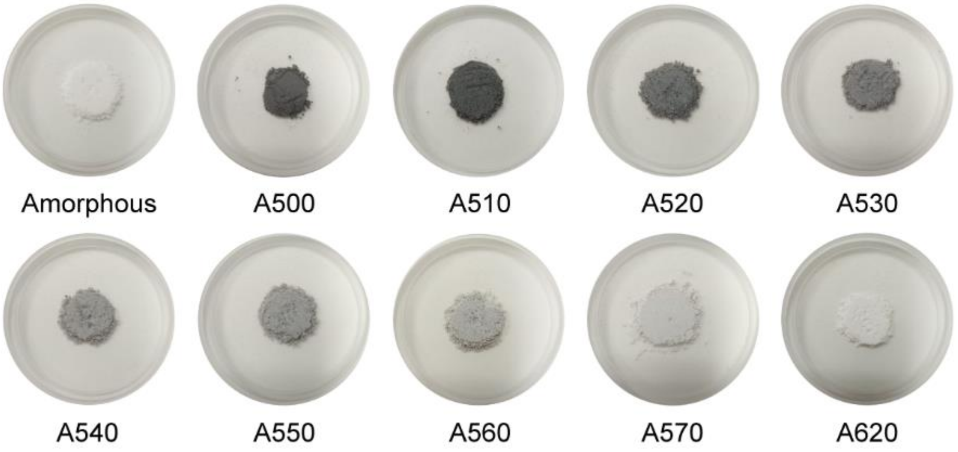

Figure A1: $Al_2W_3O_{12}$ powders from as-synthesized amorphous to calcined at 620 ºC

A2

Diffraction patterns of orthorhombic $Al_2W_3O_{12}$ powder calcined in air atmosphere at a) 540 ºC, b) 570 ºC, and c) 620 ºC. The patterns were adjusted using the Pawley method.

a)

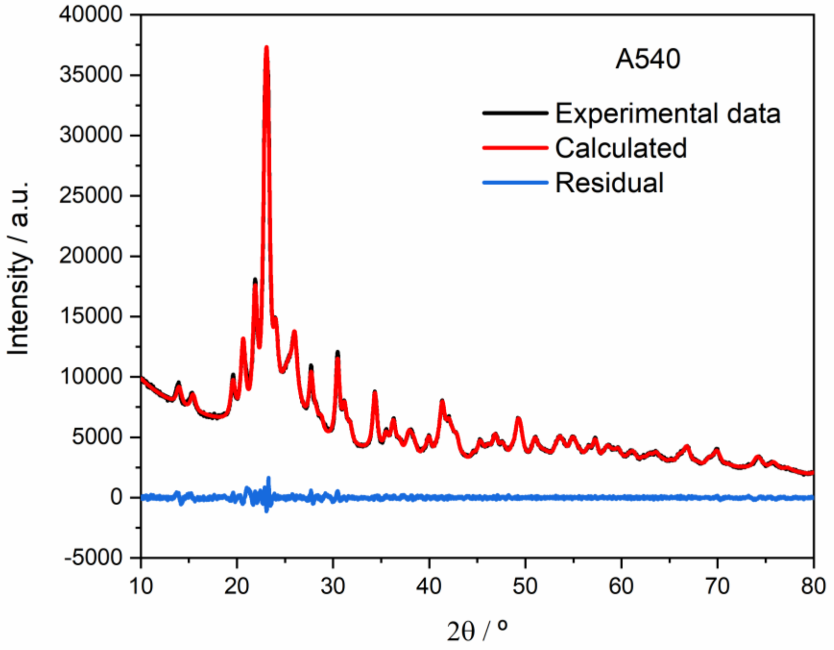
A540
Experimental data
Calculated
Residual
Intensity / a.u.
40000
35000
30000
25000
20000
15000
10000
5000
0
-5000
10
20
30
40
50
60
70
80
2θ / °

b)

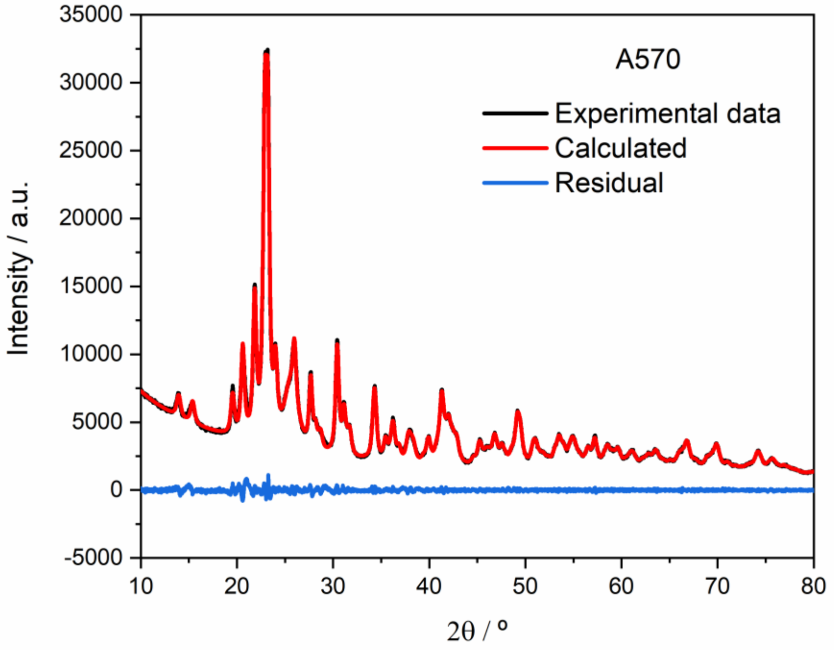
A570
Experimental data
Calculated
Residual
Intensity / a.u.
35000
30000
25000
20000
15000
10000
5000
0
-5000
10
20
30
40
50
60
70
80
2θ / °

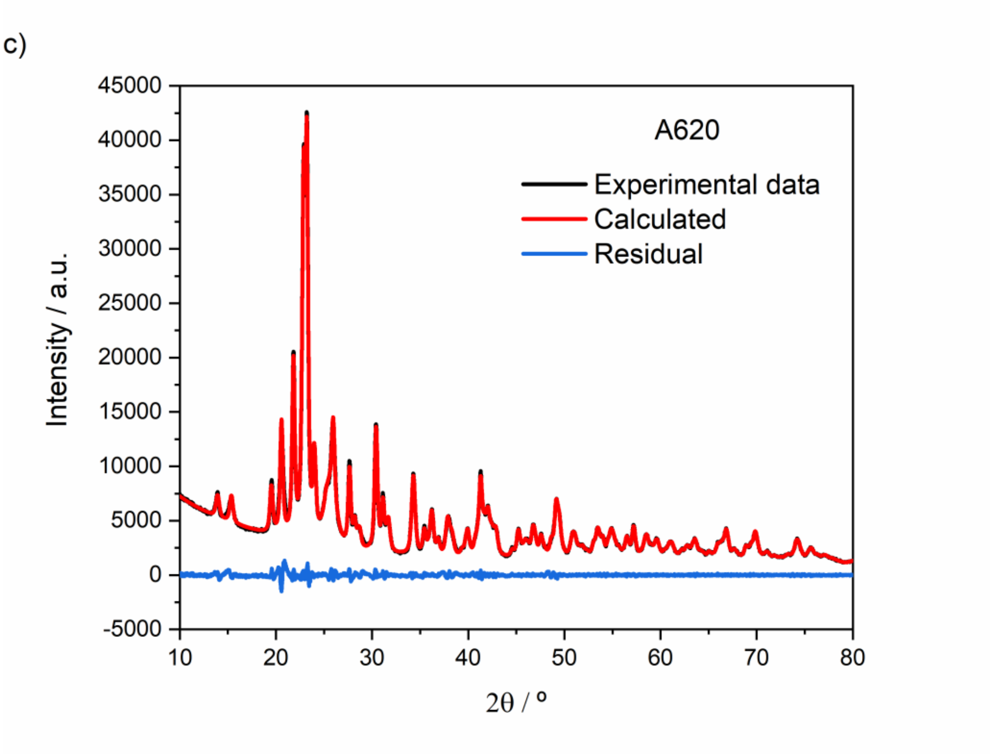

Figure A2: Diffraction patterns of orthorhombic $Al_2W_3O_{12}$ powder calcined in air atmosphere at a) 540 ºC, b) 570 ºC, and c) 620 ºC.

A3

TEM of $Al_2W_3O_{12}$-based powders calcined in air atmosphere at a) 500 ºC, b) 530 ºC and c) 620 ºC.

a)

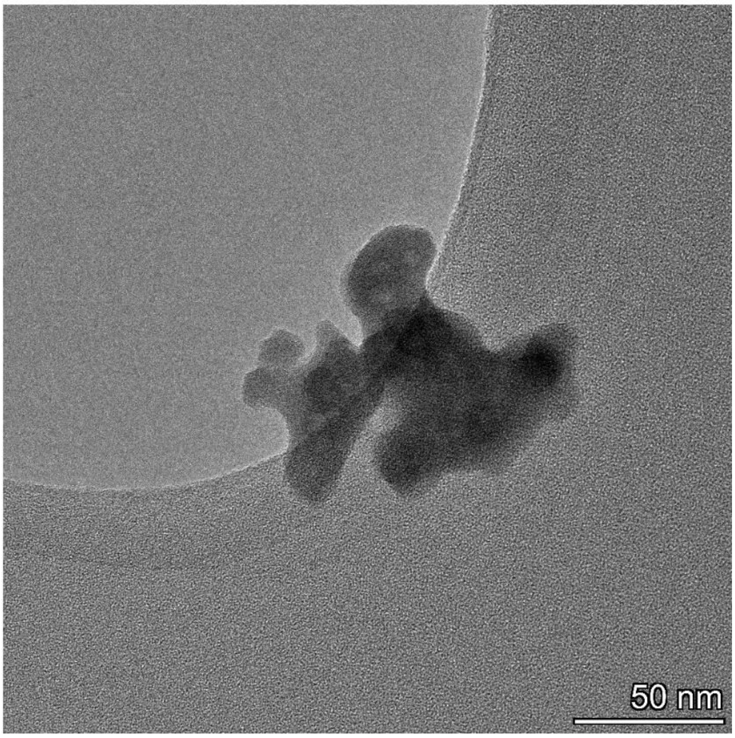

b)

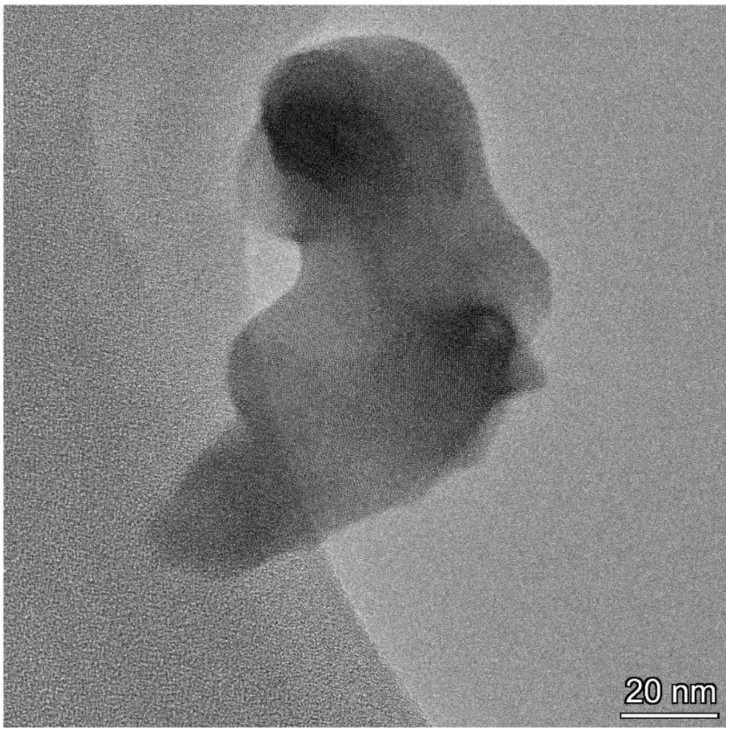

c)

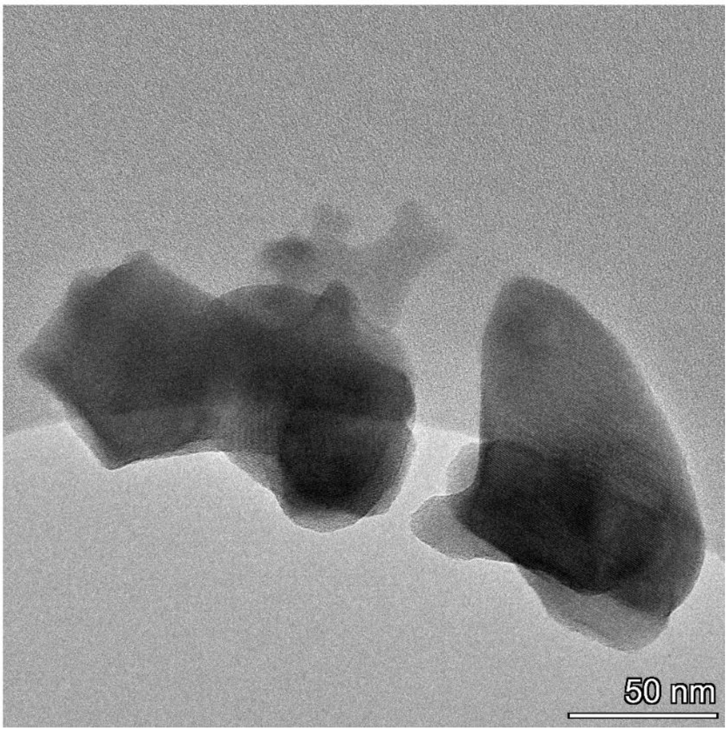

Figure A3: TEM of the $Al_2W_3O_{12}$-based powders calcined at a) 500 ºC, b) 530 ºC and c) 620 ºC.

Table A1

Unit-cell volumes of the samples calcined at 540 ºC, 570 ºC and 620 ºC acquired from XRPD patterns adjusted by the Pawley method, using Topas software, version 5.

Table A1: Unit-cell volumes of the samples A540, A570 and A620.

Sample	A540	A570	A620
Unit-cell volume (Å^3)	1048.57	1046.79	1044.86

A4

Tauc plot using Kubelka-Munk function of the $Al_2W_3O_{12}$ calcined at 620 ºC.

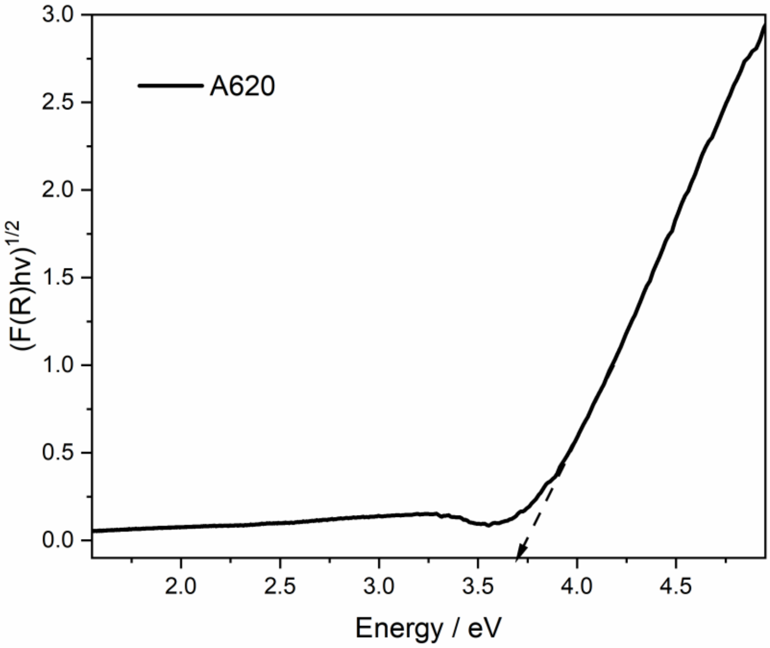

Figure A4: Kubelka-Munk of the $Al_2W_3O_{12}$-based powder calcined at 620 ºC.

Table A2

SETOV content of the amorphous powder and the powders calcined from 500 ºC to 620 º

Table A2: SETOV content of the amorphous powder and the powders calcined from 500 ºC to 620 ºC.

T (ºC)	Amorphous precursor	500	510	520	530	540	550	560	570	620
SETOV (cm^{-3})	< 10^{14}	6.66 E17	6.10 E17	4.95 E17	3.00 E17	2.24 E17	1.28 E17	7.98 E16	3.39 E16	3.48 E15

A5

The calculation of the volumetric expansion of WO_4 tetrahedra was carried out using the equation (15) for the volume of a regular tetrahedra, considering the radius of the circumference (R), as shown below.

$$V = \frac{8}{9\sqrt{3}} R^3 \qquad (15)$$

The parameter R is known as the distance from the center to the vertices, i.e., the radius of the circumference R is the distance between W and O. The R values were calculated from the redshift of symmetric stretching vibrations observed in Raman spectra (Figure 5); for the samples calcined at 540 ºC and 620 ºC, the R values were 1.6895 Å and 1.6836 Å, respectively. Therefore, a 1.06 % volumetric expansion was identified for WO_4 for the sample calcined at 540 ºC in comparison to 620 ºC.

7
References

[1] Marinkovic, B. A.; Pontón, P. I.; Romao, C. P.; Moreira, T.; White, M. A. Negative and Near-Zero Thermal Expansion in $A_2M_3O_{12}$ and Related Ceramic Families: A Review. *Front. Mater.*, **2021**, 8, 741560. https://doi.org/10.3389/fmats.2021.741560.

[2] Miller, W.; Smith, C. W.; MacKenzie, D. S.; Evans, K. E. Negative Thermal Expansion: A Review. *J. Mater. Sci.*, **2009**, 44, 5441–51. https://doi.org/10.1007/s10853-009-3692-4.

[3] Romao, C. P.; Miller, K. J.; Whitman, C. A.; White, M. A.; Marinkovic, B. A. Negative Thermal Expansion (Thermomiotic) Materials. Comprehensive Inorganic Chemistry II, 2nd ed.; *Elsevier*, **2013**, 4, 127–51. https://doi.org/10.1016/B978-0-08-097774-4.00425-3.

[4] Liu, H.; Sun, W.; Zhang, Z.; Lovings, L.; Lind, C. Thermal Expansion Behavior in the $A_2M_3O_{12}$ Family of Materials. *Solids*, **2021**, 2 (1), 87–107. https://doi.org/10.3390/solids2010005.

[5] Mączka, M.; Hermanowicz, K.; Pietraszko, A.; Yordanova, A.; Koseva, I. Structure, optical and phonon properties of bulk and nanocrystalline $Al_{2-x}Sc_x(WO_4)_3$ solid solutions doped with Cr^{3+}. *Opt. Mater.*, **2014**, 36 (3), 658–664. https://doi.org/10.1016/j.optmat.2013.11.006.

[6] Cheng, Y.; Mao, Y.; Yuan, B.; Ge, X.; Guo, J.; Chao, M.; Liang, E. Enhanced negative thermal expansion and optical absorption of $In_{0.6}(HfMg)_{0.7}Mo_3O_{12}$ with oxygen vacancies. *Phys. Lett. A*, **2017**, 381 (27), 2195–2199. https://doi.org/10.1016/j.physleta.2017.05.002.

[7] Zhang, N.; Zhou, W.; Chao, M.; Mao, Y.; Guo, J.; Li, Y.; Feng, D.; Liang, E. Negative thermal expansion, optical and electrical properties of HfMnMo2PO12-δ. *Ceram. Int.*, **2015**, 41 (10), 15170–15175. https://doi.org/10.1016/j.ceramint.2015.08.090.

[8] Dasgupta, N.; Sörge, E.; Butler, B.; Wen, T. C.; Shetty, D. K.; Cambrea, L. R.; Harris, D. C. Synthesis and characterization of $Al_{2-x}Sc_x(WO_4)_3$ ceramics for low-expansion infrared-transmitting windows. *J. Mater. Sci.*, **2012**, 47 (17), 6286–6296. https://doi.org/10.1007/s10853-012-6548-2.

[9] Moreno Diaz, E. C.; Maia Da Costa, M. E.; Paraguassu, W.; Krambrock, K.; Dosen, A.; Johnson, M. B.; White, M. A.; Marinkovic, B. A. Extrinsic Point Defects in Low-Positive Thermal Expansion $Al_2W_3O_{12}$ and Their Effects on Thermal and Optical Properties. *Inorg. Chem.*, **2022**, 61 (35), 14086–1494. https://doi.org/10.1021/acs.inorgchem.2c02113.

[10] Prisco, L. P.; Pontón, P. I.; Guamán, M. V.; Avillez, R. R.; Romao, C. P.; Johnson, M. B.; White, M. A.; Marinkovic, B. A. Assessment of the Thermal Shock Resistance Figures of Merit of $Al_2W_3O_{12}$, a Low Thermal Expansion Ceramic. *J. Am. Ceram. Soc.*, **2016**, 99 (5), 1742–1748. https://doi.org/10.1111/jace.14160.

[11] Costa, I. M.; Blair, V. L.; Paraguassu, W.; Marinkovic, B. A. Evaluating $Al_{2-x}Ga_xW_3O_{12}$ system for thermal shock resistance. *J. Solid State Chem.*, **2019**, 277, 149–158. https://doi.org/10.1016/j.jssc.2019.05.041.

[12] Prajzler, V.; Průša, S.; Maca, K. Rapid pressure-less sintering of fine grained zirconia ceramics: Explanation and elimination of a core-shell structure. *J. Eur. Ceram. Soc.*, **2019**, 39 (16), 5309–5319. https://doi.org/10.1016/j.jeurceramsoc.2019.07.053.

[13] Ernst, G.; Broholm, C.; Kowach, G. R.; Ramirez, A. P. Phonon density of states and negative thermal expansion in ZrW_2O_8. *Nature*, **1998**, 396 (6706), 147–149. https://doi.org/10.1038/24115.

[14] Romao, C. P.; Donegan, S. P.; Zwanziger, J. W.; White, M. A. Relationships between elastic anisotropy and thermal expansion in $A_2Mo_3O_{12}$ materials. *Phys. Chem. Chem. Phys.*, **2016**, 18 (44), 30652–30661. https://doi.org/10.1039/c6cp06356j.

[15] Parker, F. J.; Rice, R. W. Correlation between Grain Size and Thermal Expansion for Aluminum Titanate Materials. *J. Am. Ceram. Soc.*, **1989**, 72 (12), 2364–2366. https://doi.org/doi:10.1111/j.1151-2916.1989.tb06091.x.

[16] Sumithra, S.; Umarji, A. M. Role of crystal structure on the thermal expansion of $Ln_2W_3O_{12}$ (Ln = La, Nd, Dy, Y, Er and Yb). *Solid State Sci.*, **2004**, 6 (12), 1313–1319. https://doi.org/10.1016/j.solidstatesciences.2004.07.023.

[17] Lind, C. Two Decades of Negative Thermal Expansion Research: Where do we stand? *Materials*, **2012**, 5 (6), 1125–1154. https://doi.org/10.3390/ma5061125.

[18] Prisco, L. P.; Romao, C. P.; Rizzo, F.; White, M. A.; Marinkovic, B. A. The effect of microstructure on thermal expansion coefficients in powder-processed $Al_2Mo_3O_{12}$. *J. Mater. Sci.*, **2013**, 48, 2986–2996. https://doi.org/10.1007/s10853-012-7076-9.

[19] Truitt, R.; Hermes, I.; Main, A.; Sendecki, A.; Lind, C. Low temperature synthesis and characterization of $AlScMo_3O_{12}$. *Materials*, **2015**, 8 (2), 700–716. https://doi.org/10.3390/ma8020700.

[20] Nikolov, V.; Koseva, I.; Stoyanova, R.; Zhecheva, E. Conditions for preparation of nanosized $Al_2(WO_4)_3$. *J. Alloys Compd.*, **2010**, 505 (2), 443–449. https://doi.org/10.1016/j.jallcom.2010.06.100.

[21] Zhecheva, E.; Stoyanova, R.; Ivanova, S.; Nikolov, V. On the preparation of nanosized $Al_2(WO_4)_3$ by a precipitation method. *Solid State Sci.*, **2010**, 12 (12). https://doi.org/10.1016/j.solidstatesciences.2010.08.018.

[22] Zhang, H.; Zhang, Q.; Jia, Q. L.;, YE, G. T. Preparation of $Al_{2-x}Y_xW_3O_{12}$ powders by citrate sol-gel process. *Trans. Nonfer. Metals*

Soc. Chin., **2008**, 18 (5), 1112–1116. https://doi.org/10.1016/S1003-6326(08)60190-9.

[23] Liu, H.; Zhang, N.; Zhang, Z. Investigating negative thermal expansion property of decahedral $Sc_2Mo_3O_{12}$ prepared via hydrothermal method. *Solid State Sci.*, **2022**, 132, 106961. https://doi.org/doi.org/10.1016/j.solidstatesciences.2022.106961.

[24] Marzano, M.; Pontón, P. I.; Barreto, A. R. J.; Marinkovic, B. A. Non-hydrolytic sol-gel synthesis of $Al_2W_3O_{12}$ nanopowders. *J. Sol-gel Sci. Technol.*, **2022**, 104 (2), 267–275. https://doi.org/10.1007/s10971-022-05934-6.

[25] De Yoreo, J. J.; Vekilov, P. G. Principles of Crystal Nucleation and Growth. *Rev. min. Geochem.*, **2003**, 54 (1), 57–93. https://doi.org/10.2113/0540057.

[26] Chen, H. I.; Chang, H. Y. Homogeneous precipitation of cerium dioxide nanoparticles in alcohol/water mixed solvents. *Colloids Surf. A Physicochem. Eng. Asp.*, **2004**, 242 (1-3), 61–69. https://doi.org/10.1016/j.colsurfa.2004.04.056.

[27] Tilley, R. J. D. Defects In Solids. *John Wiley & Sons*, **2008**. https://doi.org/10.1002/9780470380758.

[28] Carter, C. B.; Norton, M. G. Ceramic materials: Science and engineering. *Springer New York*, **2013**. https://doi.org/10.1007/978-1-4614-3523-5.

[29] Li, G.; Blake, G. R.; Palstra, T. T. M. Vacancies in functional materials for clean energy storage and harvesting: The perfect imperfection. *Chem. Soc. Rev.*, **2017**, 46 (6), 1693–1706. https://doi.org/10.1039/c6cs00571c.

[30] Ragone, D. V. Thermodynamics of materials. *New York: Willey*, **1995**.

[31] Ji, Q.; Bi, L.; Zhang, J.; Cao, H.; Zhao, X. S. The role of oxygen vacancies of ABO_3 perovskite oxides in the oxygen reduction

reaction. *Energy Environ. Sci.*, **2020**, 13 (5), 1408–1428. https://doi.org/10.1039/d0ee00092b.

[32] Chen, D.; Chen, C.; Baiyee, Z. M.; Shao, Z.; Ciucci, F. Nonstoichiometric Oxides as Low-Cost and Highly-Efficient Oxygen Reduction/Evolution Catalysts for Low-Temperature Electrochemical Devices. *Chem. Rev.*, **2015**, 115 (18), 9869–9921. https://doi.org/10.1021/acs.chemrev.5b00073.

[33] Marak, V.; Ilcikova, M.; Drdlikova, K.; Drdlik, D. Plasma treatment and rapid pressure-less sintering for fabrication of environmentally friendly hydroxyapatite biocoatings. *J. Eur. Ceram. Soc.*, **2024**, 44 (4), 2590–2599. https://doi.org/10.1016/j.jeurceramsoc.2023.11.044.

[34] Barsoum, M. W. Fundamentals of Ceramics. *CRC press*, **2003**.

[35] Kang, S. J. L. Sintering: Densification, Grain Growth, and Microstructure. *Elsevier*, **2005**. https://doi.org/10.1016/B978-0-7506-6385-4.X5000-6.

[36] Yushin, D. I.; Smirnov, A. V.; Solis Pinargote, N. W.; Peretyagin, P. Y.; Torrecillas San Millan, R. Modeling process of spark plasma sintering of powder materials by finite element method. *Mater. Sci. Forum*, **2015**, 834, 41–50. https://doi.org/10.4028/www.scientific.net/MSF.834.41.

[37] Zhang, F.; Burkel, E. Novel Titanium Manganese Alloys and Their Macroporous Foams for Biomedical Applications Prepared by Field Assisted Sintering. *Biomed. Eng., Trends Mat. Sci.*, **2011**, 9, 203–224. https://doi.org/10.5772/12874.

[38] Rahaman, M. N. Ceramic Processing and Sintering. *CRC Press*, **2003**.

[39] Suarez, M.; Fernandez, A.; Menendez, J. L.; Torrecillas, R.; H. U., Hennicke J, et al. Challenges and Opportunities for Spark Plasma Sintering: A Key Technology for a New Generation of Materials. *Sin. App., InTech*, **2013**, 13, 319-342. https://doi.org/10.5772/53706.

[40] Chaim, R. Densification mechanisms in spark plasma sintering of nanocrystalline ceramics. *Mater. Sci. Eng. A*, **2007**, 443 (1-2), 25–32. https://doi.org/10.1016/j.msea.2006.07.092.

[41] Attfield, P. J. Mechanisms and materials for NTE. *Front. Chem.*, **2018**, 6, 371. https://doi.org/10.3389/fchem.2018.00371.

[42] Liu, J.; Maynard-Casely, H. E.; Brand, H. E. A.; Sharma, N. $Sc_{1.5}Al_{0.5}W_3O_{12}$ Exhibits Zero Thermal Expansion between 4 and 1400 K. *Chem. Mater.*, **2021**, 33 (10), 3823–3831. https://doi.org/10.1021/acs.chemmater.1c01007.

[43] Romao, C. P.; Dabkowski, A.; Marinkovic, B. A.; White, M. A. Thermal properties of single crystals of the low-positive thermal expansion material $Al_2W_3O_{12}$. *Solid State Commun.*, **2022**, 353, 114873. https://doi.org/10.1016/j.ssc.2022.114873.

[44] Gao, Q.; Sun, Q.; Venier, A.; Sanson, A.; Huang, Q.; Jia, Y.; Liang, E.; Chen, J.. The role of average atomic volume in predicting negative thermal expansion: The case of $REFe(CN)_6$. *Sci. China Mater.*, **2022**, 65 (2), 553–557. https://doi.org/10.1007/s40843-021-1797-3.

[45] Hu, Y.; Liu, X.; Xu, S.; Wei, W.; Zeng, G.; Yuan, H.; Gao, Q.; Guo, J.; Chao, M.; Liang, E.. Improving the Thermal Expansion and Capacitance Properties of MoO_3 by Introducing Oxygen Vacancies. *J. Phys. Chem. C*, **2021**, 125 (19), 10817–10823. https://doi.org/10.1021/acs.jpcc.1c02405.

[46] Zhang, C.; Geng, X.; Li, J.; Luo, Y.; Lu, P. Role of oxygen vacancy in tuning of optical, electrical and NO_2 sensing properties of ZnO_{1-x} coatings at room temperature. *Sens. Actuators B*, **2017**, 248, 886–893. https://doi.org/10.1016/j.snb.2017.01.105.

[47] Gil-Londoño, J.; Krambrock, K.; De Oliveira, R.; Cremona, M.; Maia Da Costa, M. E. H.; Marinkovic, B. A. Extrinsic Point Defects in TiO_2-Acetylacetone Charge-Transfer Complex and Their Effects on Optical and Photochemical Properties. *Inorg. Chem.*, **2023**, 62 (5), 2273-2288 . https://doi.org/10.1021/acs.inorgchem.2c04016.

[48] Albetran, H.; O’Connor, B. H.; Low, I. M. Effect of calcination on band gaps for electrospun titania nanofibers heated in air-argon mixtures. *Mater. Des.*, **2016**, 92, 480–485. https://doi.org/10.1016/j.matdes.2015.12.044.

[49] Fu, L.; Chen, H.; Wang, K.; Wang, X. Oxygen-vacancy generation in $MgFe_2O_4$ by high temperature calcination and its improved photocatalytic activity for CO_2 reduction. *J. Alloys Compd.*, **2022**, 891, 161925. https://doi.org/10.1016/j.jallcom.2021.161925.

[50] Bsaibess, E.; Delorme, F.; Monot-Laffez, I.; Giovannelli, F. Ultra-low thermal conductivity in scheelite and A-deficient scheelite ceramics. *Scr. Mater.*, **2021**, 201, 113950. https://doi.org/10.1016/j.scriptamat.2021.113950.

[51] Zhao, M.; Pan, W.; Li, T.; Huang, M.; Huang, Y.; Yang, J.; Li, Z.; Wan, C. Oxygen-vacancy-mediated microstructure and thermophysical properties in $Zr_3Ln_4O_{12}$ for high-temperature applications. *J. Am. Ceram. Soc.*, **2019**, 102 (4), 1961–1970. https://doi.org/10.1111/jace.16052.

[52] Duan, B.; Li, Y.; Li, J.; Gao, Y.; Zhai, P.; Yang, J.; Lu, Z.; Yang, H.; Wang, H.; Li, G. Regulation of Oxygen Vacancy and Reduction of Lattice Thermal Conductivity in ZnO Ceramic by High Temperature and High Pressure Method. *Ceram. Int.*, **2020**, 46 (16), 26176−26181. https://doi.org/10.1016/j.ceramint.2020.07.115.

[53] Li, Y.; Zhang, Y.; Zhang, N.; Li, Y.; Wu, Y. Negative thermal expansion property of $Sm_{1-x}Cu_xMnO_{3-\delta}$. *J. Mater. Res. Tech.*, **2021**, 12, 2267–2272. https://doi.org/10.1016/j.jmrt.2021.04.027.

[54] Ari, M.; Jardim, P. M.; Marinkovic, B. A.; Rizzo, F.; Ferreira, F. F. Thermal expansion of $Cr_{2x}Fe_{2-2x}Mo_3O_{12}$, $Al_{2x}Fe_{2-2x}Mo_3O_{12}$ and $Al_{2x}Cr_{2-2x}Mo_3O_{12}$ solid solutions. *J. Solid State Chem.*, **2008**, 181 (6), 1472–1479. https://doi.org/10.1016/j.jssc.2008.03.015.

[55] Zhu, J.; Yang, J.; Cheng, X. Synthesis and tunable thermal expansion property of $Al_{2-\delta}Sc_{\delta}W_3O_{12}$. *Solid State Sci.*, **2012**, 14 (1), 187–190. https://doi.org/10.1016/j.solidstatesciences.2011.11.023.

[56] Nanda Gopala Krishna, D.; George, R. P.; Philip, J. Role of Oxygen Vacancy Formation Energy and Insulating Behavior in Darkening of White Amorphous TiO_2. *J. Phys. Chem. C.*, **2021**, 125 (29), 16136–16146. https://doi.org/10.1021/acs.jpcc.1c02599.

[57] Jeong, J. H.; Lee, K.; Cho, T. S. Crystallization of amorphous TiO_2 nanotubes: A real-time synchrotron X-ray scattering study. *J. Nanosci. Nanotechnol.*, **2017**, 17 (10), 7824–7827. https://doi.org/10.1166/jnn.2017.14847.

[58] Zhang, F.; Li, H.; Cui, Y. T.; Li, G. L.; Guo, Q. Evolution of optical properties and band structure from amorphous to crystalline Ga_2O_3 films. *AIP Adv.*, **2018**, 8 (4), 045112. https://doi.org/10.1063/1.5021867.

[59] Cheary, R. W.; Coelho, A. A Fundamental Parameters Approach to X-ray Line-Profile Fitting. *J. Applied Cryst.*, **1992**, 25 (2), 108-121. https://doi.org/10.1107/s0021889891010804.

[60] Wertz, J. E.; Auzins, P. Crystal Vacancy Evidence from Electron Spin Resonance. *Phys. Rev.*, **1957**, 106 (3), 484-488 https://doi.org/10.1103/PhysRev.106.484.

[61] Walton, J.; Wincott, P.; Fairley, N.; Carrick, A. Peak Fitting with CasaXPS: A Casa pocket Book. *Accolyte Science*, **2010**.

[62] Pontón, P. I.; Prisco, L. P.; Dosen, A.; Faro, G. S.; de Abreu, M. A. S.; Marinkovic, B. A. Co-precipitation synthesis of $Y_2W_3O_{12}$ submicronic powder. *Ceram. Int.*, **2017**, 43 (5), 4222–4228. https://doi.org/10.1016/j.ceramint.2016.12.055.

[63] Pudukudy, M.; Yaakob, Z.; Rajendran, R.; Kandaramath, T. Photodegradation of methylene blue over novel 3D ZnO microflowers with hexagonal pyramid-like petals. *React. Kinet., Mech. Catal.*, **2014**, 112 (2), 527–542. https://doi.org/10.1007/s11144-014-0703-5.

[64] Gómez, I.; Otazo, E. M.; Hernández, H.; Rubio, E.; Varela, J.; Ramírez, M.; Barajas, l.; Gordillo, A. J. Thermal degradation study of PVA derivative with pendant phenylthionecarbamate groups by DSC/TGA and GC/MS. *Polym. Degrad. Stab.*, **2015**, 112, 132–136. https://doi.org/10.1016/j.polymdegradstab.2014.12.027.

[65] Woodcock, D. A.; Lightfoot, P.; Ritter, C. Negative Thermal Expansion in $Y_2(WO_4)_3$. *J. Solid State Chem.*, **2000,** 149 (1), 92-98. https://doi.org/10.1006/jssc.1999.8502.

[66] Tsvetkov, M.; Elenkova, D.; Milanova, M. Luminescence Properties of $Gd_2(MoO_4)_3$ Modified with Sm(III) and Tb(III) for Potential LED Applications. *Crystals*, **2022**, 12 (1), 120. https://doi.org/10.3390/cryst12010120.

[67] Liang, Y.; Cheng, Y. G.; Ge, X. H.; Yuan, B. H.; Guo, J.; Sun, Q.; Liang, E. J.. Negative thermal expansion and photoluminescence in solid solution $(HfSc)_{0.83}W_{2.25}P_{0.83}O_{12-\delta}$. *Chin. Phys. B*, **2017**, 26 (10), 106501. https://doi.org/10.1088/1674-1056/26/10/106501.

[68] Romao, C. P.; Miller, K. J.; Johnson, M. B.; Zwanziger, J. W.; Marinkovic, B. A.; White, M. A. Thermal, vibrational, and thermoelastic properties of $Y_2Mo_3O_{12}$ and their relations to negative thermal expansion. *Phys. Rev. B*, **2014**, 90 (2), 024305. https://doi.org/10.1103/PhysRevB.90.024305.

[69] Wan, J.; Chen, W.; Jia, C.; Zheng, L.; Dong, J.; Zheng, X.; Wang, Y.; Chen, C.; Peng, Q.; et al. Defect Effects on TiO_2 Nanosheets: Stabilizing Single Atomic Site Au and Promoting Catalytic Properties. *Adv. Mater.*, **2018**, 30 (11), 1705369. https://doi.org/10.1002/adma.201705369.

[70] Yanase, I.; Ootomo, R.; Kobayashi, H. Effect of B substitution on thermal changes of UV–Vis and Raman spectra and color of $Al_2W_3O_{12}$ powder. *J. Therm. Anal. Calorim.*, **2018**, 132 (1), 1–6. https://doi.org/10.1007/s10973-017-6933-9.

[71] Paraguassu, W.; Maczka, M.; Filho, A. G. S.; Freire, P. T. C.; Melo, F. E. A.; Filho, J. M.; Hanuza, J. A comparative study of negative thermal expansion materials $Sc_2(MoO_4)_3$ and $Al_2(WO_4)_3$ crystals. *Vib. Spectrosc.*, **2007**, 44 (1), 69–77. https://doi.org/10.1016/j.vibspec.2006.08.006.

[72] Chan, S. S.; Wachs, I. E.; Murrell, L. L. Relative Raman cross-sections of tungsten oxides: [WO_3, $Al_2(WO_4)_3$ and WO_3/Al_2O_3]. *J. Catal.*, **1984**, 90 (1), 150–155. https://doi.org/10.1016/0021-9517(84)90096-4.

[73] Hardcastle, F. D. Determination of the Molecular Structures of Tungstates by Raman Spectroscopy. *J. Raman spectrosc.*, **1995**, 26 (6), 397–405. https://doi.org/10.1002/jrs.1250260603.

[74] Chen, P.; Baldwin, M.; Bandaru, P. R. Hierarchically structured, oxygen deficient, tungsten oxide morphologies for enhanced photoelectrochemical charge transfer and stability. *J. Mater. Chem. A*, **2017**, 5 (28), 14898–14905. https://doi.org/10.1039/c7ta04118g.

[75] Liu, G.; Wang, S.; Nie, Y.; Sun, X.; Zhang, Y.; Tang, Y. Electrostatic-induced synthesis of tungsten bronze nanostructures with excellent photo-to-thermal conversion behavior. *J. Mater. Chem. A*, **2013**, 1 (35), 10120–1019. https://doi.org/10.1039/c3ta11479a.

[76] Mukhtarova, M.; Golubeva, M.; Sadovnikov, A.; Maximov, A. Guaiacol to Aromatics: Efficient Transformation over In Situ-Generated Molybdenum and Tungsten Oxides. *Catalysts*, **2023**, 13 (2), 263. https://doi.org/10.3390/catal13020263.

[77] Chao, L.; Sun, C.; Dou, J.; Li, J.; Liu, J.; Ma, Y.; Ziao, L. Tunable transparency and nir-shielding properties of nanocrystalline sodium tungsten bronzes. *Nanomaterials*, **2021**, 11 (3), 731. https://doi.org/10.3390/nano11030731.

[78] Abrahams, S. C.; Bernstein, J. L. Crystal structure of the transition-metal molybdates and tungstates. II. diamagnetic $Sc_2(WO_4)_3$. *J. Chem. Phys.*, **1966**, 45 (8), 2745–2752. https://doi.org/10.1063/1.1728021.

[79] Evans, J. S. O.; Mary, T. A.; Sleight, A. W. Negative Thermal Expansion in $Sc_2(WO_4)_3$. *J. Solid State Chem.*, **1998**, 137 (1), 148–160. https://doi.org/10.1006/jssc.1998.7744.

[80] Evans, J. S. O.; Mary, T. A. Structural phase transitions and negative thermal expansion in $Sc_2(MoO_4)_3$. *Inter. J. Inorg. Mater.*, **2000**, 2 (1), 143-151. https://doi.org/10.1016/S1466-6049(00)00012-X.

[81] Marinkovic, B. A.; Ari, M.; De Avillez, R. R.; Rizzo, F.; Ferreira, F. F.; Miller, K. J.; . Correlation between AO_6 polyhedral distortion and negative thermal expansion in orthorhombic $Y_2Mo_3O_{12}$ and related materials. *Chem. Mater.*, **2009**, 21 (13), 2886–2894. https://doi.org/10.1021/cm900650c.

[82] Cheng, Y.; Liang, Y.; Ge, X.; Liu, X.; Yuan, B.; Guo, J.; Chao, M.; Liang, E. A novel material of $HfScMo_2VO_{12}$ with negative thermal expansion and intense white-light emission. *RSC Adv.*, **2016**, 6 (59), 53657–53661. https://doi.org/10.1039/c6ra09666b.

[83] Ge, X.; Liu, X.; Cheng, Y.; Yuan, B.; Chen, D.; Chao, M.; Guo, J.; Wang, J.; Liang, E. Negative thermal expansion and photoluminescence properties in a novel material $ZrScW_2PO_{12}$. *J. Appl. Phys.*, **2016**, 120 (20), 205101. https://doi.org/10.1063/1.4968546.

[84] Cao, C.; Wei, S.; Zhu, Y.; Liu, T.; Xie, A.; Noh, H. M.; Jeong, J. H. Synthesis, optical properties, and packaging of Dy^{3+} doped Y_2WO_6, $Y_2W_3O_{12}$, and Y_6WO_{12} phosphors. *Mater. Res. Bull.*, **2020**, 126, 110846. https://doi.org/10.1016/j.materresbull.2020.110846.

[85] Xu, H.; Liu, R.; Zhang, S.; Deng, M.; Han, K.; Xu, B.; Ouyang, C.; Zhong, S. Scandium Molybdate Microstructures with Tunable Phase and Morphology: Microwave Synthesis, Theoretical Calculations, and Photoluminescence Properties. *Inorg. Chem.*, **2019**, 58 (4), 2491–2500. https://doi.org/10.1021/acs.inorgchem.8b03056.

[86] Zou, H.; Yang, X.; Chen, B.; Du, Y.; Ren, B.; Sun, X.; Qiao, X.; Zhang, Q.; Wang, F. Thermal Enhancement of Upconversion by

Negative Lattice Expansion in Orthorhombic $Yb_2W_3O_{12}$. *Angewandte Chemie.*, **2019**, 58 (48), 17255–17259. https://doi.org/10.1002/anie.201910277.

[87] Zhou, Y.; Cheng, Y.; Huang, Q.; Xu, J.; Lin, H.; Wang, Y. Abnormal thermally enhanced upconversion luminescence of lanthanide-doped phosphors: proposed mechanisms and potential applications. *J. Mater. Chem. C*, **2021**, 9 (7), 2220–2230. https://doi.org/10.1039/d0tc05759b.

[88] Schulz, B.; Andersen, H. L.; Al Bahri, O. K.; Johannessen, B.; Liu, J.; Primig, S.; Sharma, N. Electrochemical performance and structure of $Al_2W_{3-x}Mo_xO_{12}$. *Cryst. Eng. Comm.*, **2018**, 20 (10), 1352–1360. https://doi.org/10.1039/c7ce01707c.

[89] Trunec, M.; Maca, K. Compaction and pressureless sintering of zirconia nanoparticles. *J. Am. Ceram. Soc.*, **2007**, 90 (9), 2735–2740. https://doi.org/10.1111/j.1551-2916.2007.01781.x.

[90] Oberacker, R. Powder Compaction by Dry Pressing. *Ceramics Sci. Technol*, **2012**, 3, 3–37. https://doi.org/10.1002/9783527631957.ch1.

[91] Kuang, X.; Carotenuto, G.; Nicolais, L. A Review of Ceramic Sintering and Suggestions on Reducing Sintering Temperatures. *Adv. Perform. Mater.*, **1997**, 4, 257–274. https://doi.org/10.1023/A:1008621020555.

[92] Prisco, L. P.; Marzano, M.; Pontón, P. I.; Costa, A. M.; da Costa Neto, C. A.; Sweet, G.; et al. Relationship between sintering methods and physical properties of the low positive thermal expansion material $Al_2W_3O_{12}$. *Int. J. Appl. Ceram. Technol.*, **2019**, 16 (1), 346–356. https://doi.org/10.1111/ijac.13054.

[93] Koseva, I.; Yordanova, A.; Nikolov, V. High-Density Ceramics of $Al_{2-x}Me_x(WO_4)_3$, (Me = Sc or In) Solid Solutions. *New J. Glass Ceram.*, **2013**, 3 (4), 104–110. https://doi.org/10.4236/njgc.2013.34017.

[94] Zhou, L.; Zhang, H.; Zhang, Z. Homogeneous nanoparticle dispersion prepared with impurity-free dispersant by the ball mill technique. *Particuology*, **2013**, 11 (4), 441–447. https://doi.org/10.1016/j.partic.2013.01.001.

[95] Tomasi, R.; Rabelo, A. A.; Chinelatto, A. S. A.; Reis, L.; Botta Fo, W. J. Characterization of high-energy milled alumina powders. *Cerâmica*, **1998**, 44, 166–170. https://doi.org/10.1590/s0366-69131998000500003.

[96] Yang, M.; Guo, Z.; Xiong, J.; Liu, F.; Qi, K. Microstructural changes of (Ti,W) C solid solution induced by ball milling. *Int. J. Refract. Metals Hard Mater.*, **2017**, 66, 83–87. https://doi.org/10.1016/j.ijrmhm.2017.03.008.

[97] Jardim, P. M.; Garcia, E. S.; Marinkovic, B. A. Young's modulus, hardness and thermal expansion of sintered $Al_2W_3O_{12}$ with different porosity fractions. *Ceram. Int.*, **2016**, 42 (4), 5211–5217. https://doi.org/10.1016/j.ceramint.2015.12.045.

[98] Olevsky, E. A.; Kandukuri, S.; Froyen, L. Consolidation enhancement in spark-plasma sintering: Impact of high heating rates. *J. Appl. Phys.*, **2007**, 102, 114913. https://doi.org/10.1063/1.2822189.

[99] García DE, Hotza D, Janssen R. Building a sintering front through fast firing. Int J Appl Ceram Technol 2011;8:1486–93. https://doi.org/10.1111/j.1744-7402.2011.02609.x.

[100] Yordanova, A. S.; Nikolov, V. S.; Koseva, I. I. Fabrication of High Density Ceramic from $Al_{2-x}In_x(WO_4)_3$ Solid Solutions. *J. Chem. Techol. Mettalurgy*, **2015**, 50 (4), 537-542.

[101] Imanaka, N.; Hiraiwa, M.; Adachi, G.; Dabkowska, H.; Dabkowski, A. Thermal contraction behavior in $Al_2(WO_4)_3$ single crystal. *J. Crystal Growth*, **2000**, 220 (1-2), 176-179. https://doi.org/10.1016/S0022-0248(00)00771-5.

[102] Wollmershauser, J. A.; Feigelson, B. N.; Gorzkowski, E. P.; Ellis, C. T.; Goswami, R.; Qadri, S. B.; et al. An extended hardness limit in

bulk nanoceramics. *Acta Mater.*, **2014**, 69, 9–16. https://doi.org/10.1016/j.actamat.2014.01.030.